EVALUATION OF QUASICRYSTAL AL-CU-FE ALLOYS FOR TRIBOLOGICAL APPLICATIONS

A Thesis

by

NEZAR DERAR NABELSI

Submitted to the Office of Graduate Studies of
Texas A&M University
in partial fulfillment of the requirements for the degree of

MASTER OF SCIENCE

Chair of Committee,	Hong Liang
Committee Members,	Ibrahim Karaman
	Jun Zou
Head of Department,	Andreas Polycarpou

August 2013

Major Subject: Mechanical Engineering

ABSTRACT

This research investigated the tribological performance of a composite material, formed from an ultra high molecular weight polyethylene (UHMWPE) matrix and quasicrystalline Al-Cu-Fe alloy powders. An evaluation was conducted for the microstructure, material properties, and tribological performance of quasicrystalline materials formed from Al-Cu-Fe alloys. Arc melting was used as the fabrication technique for these alloys, and some samples were additionally heat treated in an argon environment. Vickers microhardness testing was done to make comparisons to wear rate behavior of the various alloys. Tribological studies were conducted using a linear pin-on-desk configuration to evaluate friction and wear.

Research indicated the annealed samples of Al-Cu-Fe that formed icosahedral quasicrystalline phases, where the quasicrystalline phase was most dominant of the observed alloys, displayed the greatest wear resistance and hardness. Abrasive wear was observed in each of the samples, as the brittle, hard nature of the quasicrystalline phase would not allow for the ductile adhesion. The addition of small amounts of Al-Cu-Fe quasicrystalline particles, crushed and pulverized from the arc-melted ingots, reduced the coefficient of friction and wear rate of UHMWPE, when added to the polymer.

ACKNOWLEDGEMENTS

I would like to thank my committee chair, Dr. Hong Liang, and my committee members, Dr. Ibrahim Karaman and Dr. Jun Zou, for the time and resources they have contributed to the completion of this research, as well as the progress in my degree.

In addition, I would like to thank Xingliang He, Sukbae Joo, Yan Zhou, Brian Franco, Nick Barta, Jim Sajewski, Fevzi Ozaydin and all the other individuals who have helped me become acquainted with the use of equipment, various research methods, and the numerous tasks involved in my research.

Thanks also go to my friends and colleagues and the department faculty and staff for making my time at Texas A&M University a great experience. In addition, I would like to thank the Department of Mechanical Engineering at Texas A&M University, Chevron Corporation, the trust of the G H Thompson Graduate Fellowship, and the other groups and organizations responsible for providing the financial resources for me to complete my work and graduate studies.

Finally, I would like to thank my family for their continued support and encouragement, and I want to thank God for providing me the resources and opportunity to pursue this research.

NOMENCLATURE

AFM	Atomic force microscope
EDS	Energy-dispersive spectroscopy
HV	Vickers hardness
QC	Quasicrystal
SEM	Scanning electron microscope
TAMU	Texas A&M University
UHMWPE	Ultra high molecular weight polyethylene
XRD	X-ray diffraction

TABLE OF CONTENTS

Page

LIST OF FIGURES

Page

LIST OF TABLES

Page

CHAPTER I

INTRODUCTION

This chapter provides the necessary background to understand concepts related to quasicrystalline materials, composite materials, and tribology, the topics of interest in this research. First, the history of the discovery and use of quasicrystalline materials is discussed. The potential impact of quasicrystalline materials, as engineering materials, is also examined in this chapter. Next, the methods by which quasicrystalline materials may be synthesized are described. The mechanisms for the properties and behavior of quasicrystalline materials are described. In addition, an introduction to tribology and its significance is provided. The use of ultra high molecular weight polyethylene (UHMWPE), including UHMWPE-matrix composites, in biomedical applications is then discussed in detail.

1.1 History of Quasicrystalline Materials

The earliest discoveries related to quasicrystalline materials were in the Islamic art and architecture of the period from the 13th to 15th century, in what are known as girih tiles [1]. As the art form evolved from a pattern of networking zigzag lines to complex periodic patterns, designers were able to construct elaborate, nearly perfect Penrose patterns, the two-dimensional geometric representations of quasicrystalline structures [2]. This is particularly impressive, considering it wasn't until the 20th century that Sir Roger Penrose, the man whose name is associated with the discovery of the theory of

these semi-periodic geometric patterns, became the first westerner to explore the concept [3]. Dr. Penrose found that the use of two tiles to cover a plane would result in a semi-periodic geometry, which became the first tilings to show fivefold, rotational symmetry and the basis for representing an icosahedral quasicrystalline phase. An example of these tiles may be seen in Figure 1.

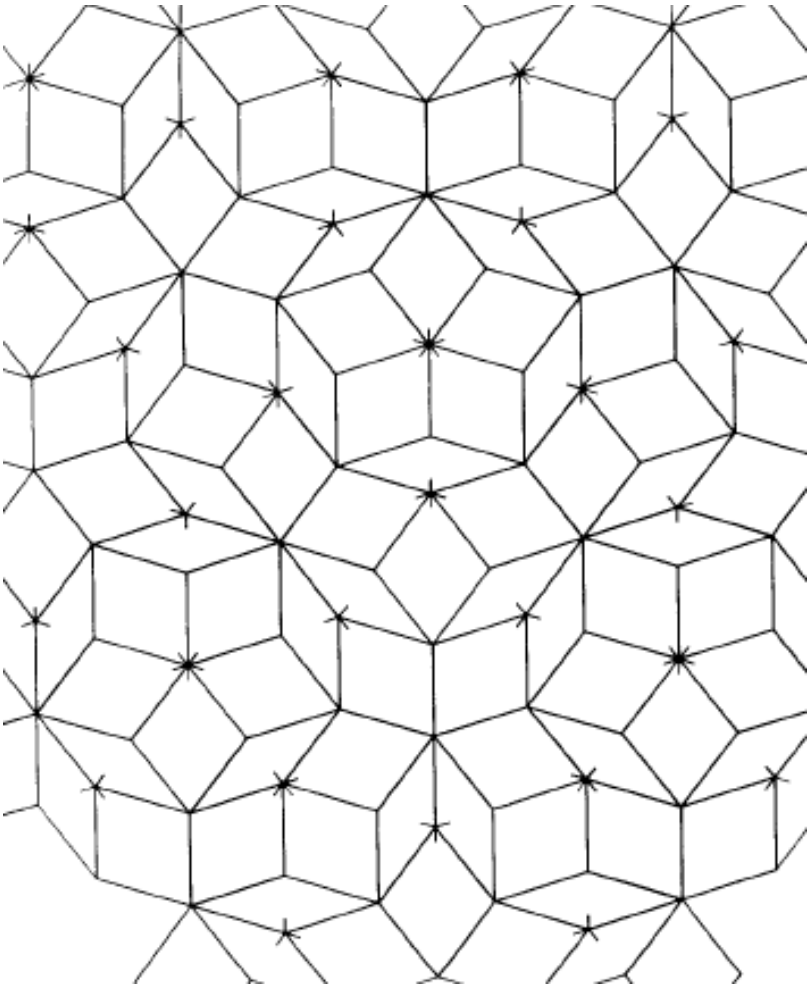

Figure 1. Penrose tiles composed from 2 rhombuses [4]

It was the research of Dan Shechtman and others, published in the paper titled "Metallic Phase with Long-Range Orientational Order and No Translational Symmetry" in 1984, which marks the beginning of the research of quasicrystals [5]. Although discovered two years prior to publishing, the group's research and findings received a great deal of skepticism and was largely ignored by many of their peers. From a rapidly cooled Al-Mn alloy sample, Shechtman and fellow researchers observed a diffraction pattern showing a relatively unusual five-fold symmetry. Shortly after publishing these finding, Ishimasa and coauthors submitted a paper titled "New ordered state between crystalline and amorphous in Ni-Cr particles", in which twelve-fold symmetry was reported [6]. Prior to these discoveries, research was conducted on similar Al-Cu-Fe alloys, though the semi-periodic nature of their structure was not understood [7]. Beginning with the work of Tsai et. al., an improved understanding of the icosahedral quasicrystalline phase present in certain Al-Cu-Fe alloys has unfolded [8, 9].

More recently, the first discovery of a natural quasicrystal, a mineral named icosahedrite and found within the rock khatyrkite, was found to have a composition of $Al_{63}Cu_{24}Fe_{13}$ [10]. This was particularly interesting, considering it was a composition similar to the earliest discovered stable quasicrystal. In addition, this composition is similar to the one that will be of interest in the present research.

Several quasicrystal structures have been observed, including icosahedral, decagonal, dodecagonal, and octagonal structures. The most commonly observed structure, and the structure seen in Al-Cu-Fe alloy quasicrystals, is the icosahedral structure. This structure has a 20-sided geometry, and they will be aperiodic in all

directions, meaning their structure will not repeat along any axis [11]. Due to this unique structure, they exhibit very unique electrical and mechanical properties. Figure 2 shows an image of an icosahedral quasicrystal, observed by SEM.

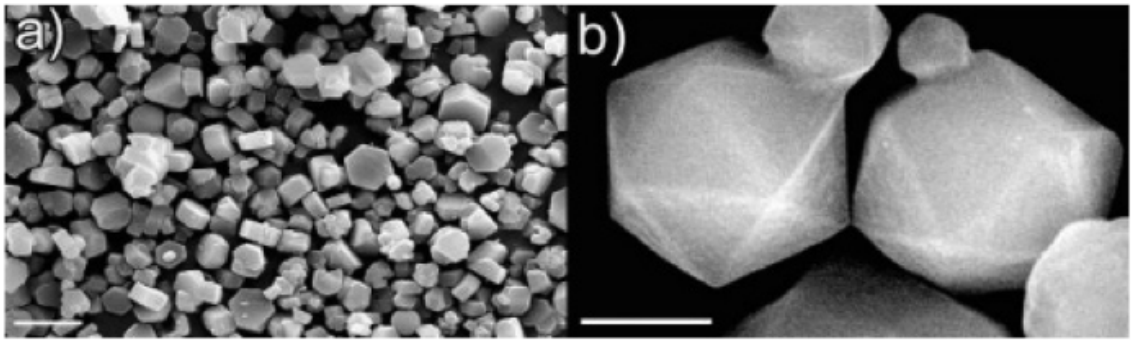

Figure 2. SEM images of icosahedral quasicrystals. Scale bar is 10 and 2 μm in a) and b), respectively [12].

1.2 Quasicrystalline Materials

1.2.1 Potential Uses and Benefits

Since, quasicrystalline materials are extremely brittle at room temperature, they have practical limitations for use as bulk materials, but they may be usable as coatings [13, 14]. Their excellent tribological behavior allows them to be excellent for use in biomedical applications, such as part of a composite material for joint replacements. When included as a microconstitutent in polymer-based composites for acetabular cup prosthetics, the presence of quasicrystalline materials has been shown to improve the wear resistance of implants [15]. Another important characteristic is their very low heat

conductivity, which makes these materials ideal thermal insulators [16, 17]. In addition, their low electrical conductivity may make them suitable for electrical biomedical devices and semiconductor manufacturing. Figure 3 shows an image of an acetabular cup prosthetic, seated in the acetabula.

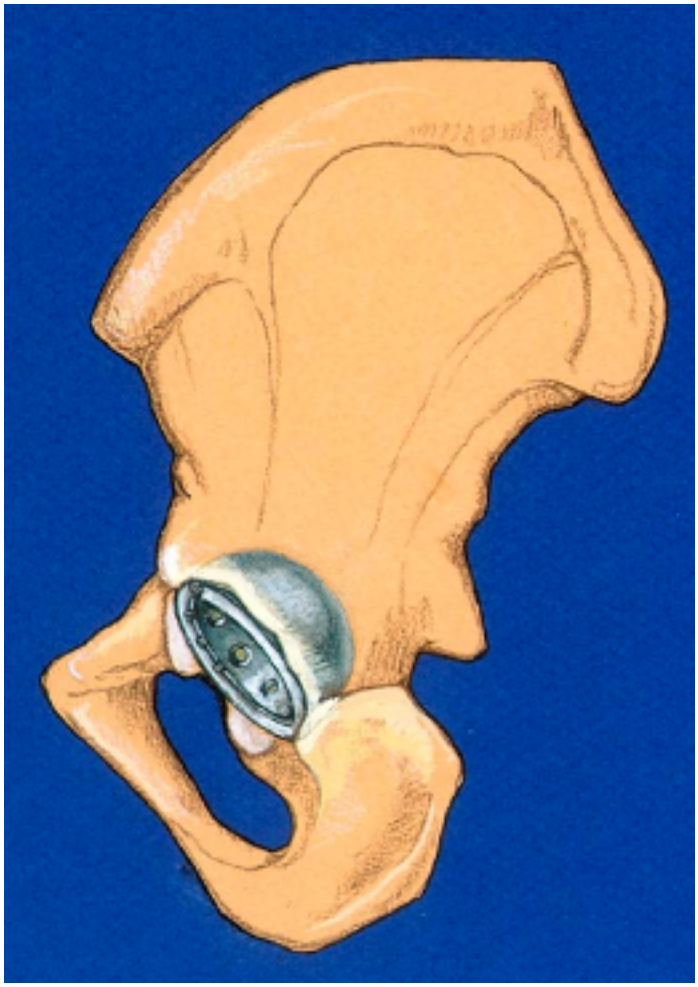

Figure 3. Prosthetic cup to connect to artificial femur joint in hip replacement [18]

1.2.2 Synthesis

Much of the focus of research on quasicrystals has had to do with their synthesis. Methods for synthesizing quasicrystals have included high-energy ball milling, laser cladding, and arc melting. The most frequently used method has appeared to be high-energy ball milling, as the majority of research related to the formation of quasicrystals has utilized this synthesis method [19-23]. Essentially, ball milling works by spinning a vacuumed, or argon-filled, canister for several hours. This canister contains the powders being alloyed, as well as metallic balls to assist the alloying process. A typical mass ratio of balls to powders could be on the order of 30:1. In order to achieve highly quasicrystalline powders, though, an annealing process is necessary.

In the case of laser cladding, this is generally done with powders that were previously measured to the appropriate atomic weights and thoroughly mixed for improved homogeneity. Laser cladding has been used more in instances where it is desirable to directly coat a substrate with the quasicrystalline materials [24-26].

Arc melting, on the other hand, has been used less frequently for forming quasicrystalline materials, but it has proven to be an effective method [27, 28]. In instances where a solid sample is desired, in order to perform tests evaluating the individual behavior of the materials, arc melting is a desirable processing method. The arc melting process will be explained in more detail in the "Methodology" portion of this proposal. Based on the above discussion, a summary of these methods used for synthesizing quasicrystals is shown in Table 1.

Table 1. Summary of methods for synthesizing quasicrystals [19-28]

Method	Description	Pros	Cons
Ball Milling	Metallic powders placed in argon-filled, or vacuumed, canister with metal balls and spun at high rotational speed for hours	Final product is in powder form, if desired; requires little energy; oxidation less likely to occur	Requires annealing after milling to get fully QC powders; contamination by metal balls, or canister; time consuming
Laser Cladding	Metal powders are placed underneath a laser beam to be melted onto a substrate	Can be used for many materials; sample can be made to almost any shape; practical for forming composites	High energy system and costly; systems sensitive to slight changes and can affect outcome of final composition
Arc Melting	Metallic pieces, or powders, placed in argon atmosphere and melted by electric arc to form solid ingot	Final product is solid ingot, if desired; requires little time and can be used for almost any metal combination; simple use	Rough exterior surface; oxide layer will often form around sample exterior; basic shapes formed

The range of stability for these alloys is relatively narrow. From Figure 4, it may be seen that the icosahedral quasicrystalline phase of an Al-Cu-Fe alloy will be limited in composition to 60-66 at.% Al, 20-26 at.% Cu, 12.5-17.5 at.% Fe. However, the formation of this phase has been seen in Al concentrations as high as 70 at.% and Fe concentrations as low as 10 at.%, after annealing the samples [29].

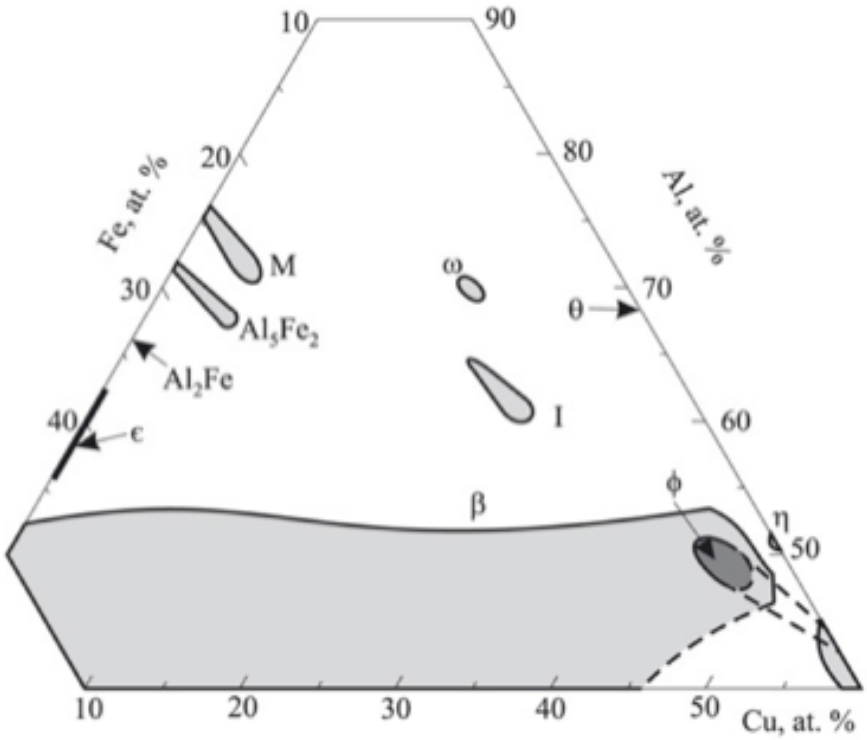

Figure 4. Ternary phase diagram for Al-Cu-Fe [30]

1.3 Tribology

Derived from the Greek word "tribos", meaning rubbing, tribology is the study of rubbing surfaces. The term tribology applies to the theory and study of contacting surfaces in relative motion [31]. Tribology covers all aspects of sliding surfaces in contact with one another, including friction, lubrication systems, bearing design and wear behavior.

1.3.1 Friction

Friction is a broad concept of a force that resists the motion of two contacting bodies, moving relative to each other. It encompasses the sliding forces of viscous flow

(fluid-to-fluid contact), dry friction (solid-to-solid contact), lubricated friction (solid-to-fluid-to-solid contact), as well as any other force resulting from relative motion. As a parameter to describe the friction behavior of an interface, the coefficient of friction is used. The coefficient of friction is a dimensionless constant, which characterizes the ability of two surfaces to slide over each other. In the case of solid-to-solid contact, this coefficient would describe the ability of two solid materials to slide, while in contact with each other. The static coefficient of friction, μ_s, may be defined as the ratio between the friction force (F_f) created by the two surfaces sliding across each other in contact, divided by the normal force (F_N) that exists between the two bodies. This relationship is shown in Equation 1 [32].

$$\mu_s = \frac{F_f}{F_N} \qquad \text{Eq. 1}$$

1.3.2 Wear

Wear studies are a relatively new field, and empirical and scientific studies of wear were relatively undeveloped before the middle of the 20th century. As of late, the emergence of advanced sensors and computational tools has allowed systematic investigations of interfacial behavior, using high resolution. The development of microtribology, or nanotribology, has also been spawned from these advances. Wear, the result of friction between two surfaces rubbing against each other, is a major limiting factor in the long-term viability of materials and equipment. Wear describes the gradual loss of material from a surface, and it may include abrasion, adhesion, erosion, surface

fatigue, or fretting wear [33].

There are many equations for evaluating wear rate, and all are based on the Archard equation. The equation is simple to use and understand, and it is based on the principle that the asperities of contacting surfaces will cause wear and friction. In Equation 2, Q is the volume of worn material, K is a dimensionless constant, W is the load, L is the total distance the surfaces will slide against each other, and H is the softer surface's hardness [34].

$$Q = \frac{KWL}{H} \qquad \text{Eq. 2}$$

This equation does not describe the specific wear behavior of the materials, though. Wear behavior can be broken down into five main mechanisms: abrasion, third body, adhesion, fatigue, and corrosion [35-37]. During abrasive wear, asperities on the harder surface will cut grooves into the softer surface. Abrasive wear results in the dislocation and removal of the softer material from the grooves created by the asperities, as the surfaces slide past each other in relative motion. Third-body wear may be described as a form of abrasive wear, but it involves the deposition of hard particles into the surface of the softer material. Adhesive wear occurs when the atomic bonding forces occurring between the surfaces of the materials in contact overcome the differing material properties, such as the bonding of asperities from opposite surfaces. As relative motion of the surfaces continues, bonds are broken, and wear particles are formed from the softer material. Fatigue wear occurs when a material's fatigue limit is overcome by cyclic shear stresses. Corrosive wear is similar to third body wear, as removed corrosive

debris acts will abrade a third body. In turn, the removed corroded debris will leave more of the surface vulnerable to further corrosion, and the rate of removal of more material will increase. Figure 5 provides an schematic diagram of wear by adhesion, abrasion, and fatigue.

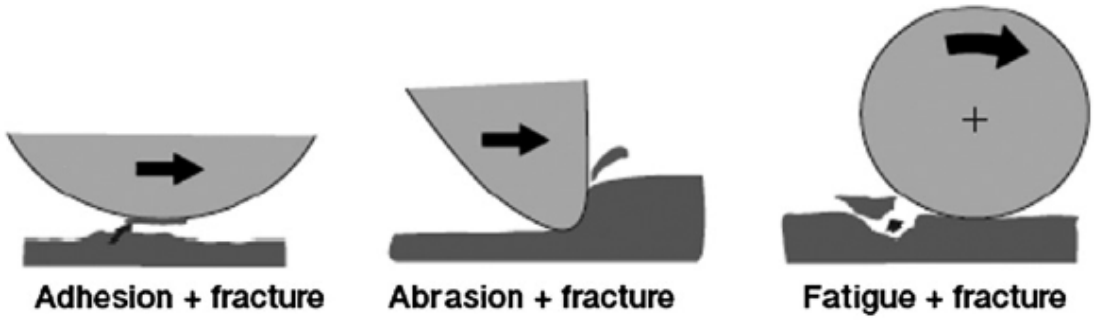

Figure 5. Schematic diagram of wear by adhesion, abrasion, and fatigue [38]

It is estimated that the economic impact of losses due to wear reside in a range of 1-2% of annual GDP [39]. In addition, estimates of annual energy losses place approximately one-third of these losses as the result of friction. Thus, the significant economic impact of improving the wear and friction behavior of materials and mechanical equipment is apparent.

1.4 Ultra High Molecular Weight Polyethylene

Ultra high molecular weight polyethylene (UHMWPE) is a form of polyethylene, a polymer with the chemical formula $(C_2H_4)_n$, having a molecular weight greater than approximately 2,000,000 g/mol. UHMWPE has been a frequently used material in the

field of biomedical joint replacements [40-43]. This is largely due to the materials' low toxicity, high strength, and low coefficient of friction. The tribological behavior of UHMWPE has been frequently investigated, as it is a critical in the assessment of the material's viability in joint replacements [44-48]. Processing these materials may be done by a variety of methods, including compression molding, injection molding, and laser powder sintering [49-51]. Compression molding, due to the ease of the manufacturing process, will be used in this research. This processing method is described in more detail in the "Experimental" chapter of this paper.

UHMWPE has been investigated for its use as a matrix material in composites, as well. With the addition of carbon nanotubes, the wear resistance of UHMWPE was shown to improve [52]. In addition, it has been observed that the addition of quasicrystals to UHMWPE has a considerably positive impact on the reduction of the material's wear rate [15, 53].

CHAPTER II

MOTIVATIONS AND OBJECTIVES

This research will explore the morphology, hardness, friction behavior, and wear resistance of an aluminum-copper-iron (Al-Cu-Fe) alloy. In addition, this work will determine the improvement in these properties and behaviors, as a measure of the amount of icosahedral quasicrystalline phase present in the alloys. It is desired to explore the impact that these alloys may present on the tribological performance of a composite containing an ultra high molecular weight polyethylene (UHMWPE) matrix, reinforced by the Al-Cu-Fe alloy. The outcome of this work is to introduce an inexpensive and novel process of synthesizing UHMWPE-Al-Cu-Fe composites.

The findings produced from this research will hopefully contribute to an expanding field of work, related to quasicrystalline materials. Showing the tribological capacities of these materials may provide further evidence for their use in industrial coatings, as well as their ability to be used as constituents of composites in biomedical applications. Although quasicrystalline materials have been explored as composite constituents in biomedical applications, the research on the subject has been limited. In addition, research has proven the electrically resistive nature of quasicrystalline materials. Thus, the findings of this research may be beneficial in applications where the electrically resistive nature and strong tribological performance of a UHMWPE-Al-Cu-Fe composite may be of interest. Example applications of this may include semiconductor manufacturing, medical electronics, and automotive components.

CHAPTER III

EXPERIMENTAL

The experimental procedures used during the course of this research project are described in this chapter. Within this chapter, details are given on the materials used and the devices and manner by which they were processed. In addition, the methods and equipment for characterization of these materials are detailed.

Material selection and preparation will be covered in the first portion of this chapter, as it is the basis for most of the work to follow. The synthesis of an Al-Cu-Fe alloy, containing a quasicrystalline phase, will be explained, as well as the synthesis of a polyethylene sample.

The development of a polyethylene-quasicrystalline alloy composite will also be discussed. This will include describing how the metal powders were made, as well as how mixing the powders and forming the final composite were achieved.

The preparation of the samples for materials characterization and analysis of properties will be briefly discussed. This is of importance, as the materials require some advanced preparation for tests, such as X-Ray Diffraction (XRD) analysis.

Finally, materials characterization methods will be discussed. This will provide background information on various testing methods employed in this research (e.g. tribometry, XRD). In addition, a thorough explanation of the process and parameters for the tests performed will be discussed, as these parameters affect the eventual state of results.

3.1 Materials

It is the aim of this research to synthesize a relatively novel material, in order to study its individual tribological behavior, as well as how its presence in a UHMWPE matrix composite affects the tribological behavior of UHMWPE. The formation of a quasicrystalline phase may be achieved through the use of an aluminum alloy, containing two other transition metals. Iron and copper were selected as these transition metals for the relatively low cost of the materials, their low toxicity when alloyed, and the fact that they had been researched more extensively than other quasicrystalline-forming alloys. Since the research available on the topic of quasicrystalline alloys is still limited, having more background information was important. High purity materials were important, as this would reduce the likelihood of oxidation and contamination. Table 1 shows the important properties of the metallic elements used in this research.

Table 2. Properties of metallic elements used in current research

Name	Aluminum	Copper	Iron
Abbreviation	Al	Cu	Fe
Atomic Number	13	29	26
Periodic Classification	Poor Metal	Transition Metal	Transition Metal
Melting Point	660.32°C	1084.62°C	1538°C
Density (@ r.t.)	2.70 g/cm^3	8.96 g/cm^3	7.87 g/cm^3
Purity	99.7%	99.9%	99.97%

Ultra high molecular weight polyethylene was chosen for investigation, as the composite matrix material. This was done because of the material's low friction coefficient, relatively good thermal stability, low toxicity, and relatively good wear resistance, with respect to other polymers. The UHMWPE used in these experiments was ordered from Sigma Aldrich, and it arrived in the form of a fine, white powder. The molecular weight of the UHMWPE used in these experiments ranged from 3,000,000-6,000,000, the melting temperature was 138°C, and the density was 0.94 g/mL at 25°C.

3.1.1 Arc Melting (Al-Cu-Fe Synthesis)

In order to successfully synthesize an Al-Cu-Fe alloy containing an icosahedral phase, several methods had been proposed. The predominant methods selected by researchers have been sintering, mechanical alloying, and arc melting. In the case of sintering, it may lead to a heavily porous structure, requires a relatively homogeneous mixing of powders, and can be very time consuming, as it is dependent on the diffusion of atoms. Mechanical alloying is a process by which fine metal powders are placed in a vacuum-sealed container with metal bearings, where the bearings far outweigh the powders (e.g. 100:1), and the container experiences a large amount of mechanical energy (e.g. spinning, shaking) for an extended period of time. Mechanical alloying had both positive and negative attributes as a synthesis method. From a positive perspective, it has been a proven method in forming the icosahedral phase of desire and produces a powder that may be easily added to a polymer powder matrix to make composites. The downsides of this method include the fact that it is very time consuming, the metal

bearings may cause contamination, and the final product will be a powder. Although a powder is desirable for mixing into the UHMWPE matrix to form a composite, it would present an issue for doing tribology tests of the alloy. The obstacle of needing powders would be better resolved by later crushing arc melted samples with a mechanical press and refining the size of the powders by using a mortar and pestle to grind the materials. Arc melting, on the other hand, was a relatively quick process to get phase results similar to mechanical alloying, with the added benefit of the final sample being a single, solid ingot. Thus, arc melting was selected as the alloy synthesis method to be used for this research. Arc melting works by the creation of an electrical arc between an electrode and the sample being melted. In order to do this, air is removed from the chamber where the melting is being done, in order to avoid material oxidation. The air is replaced with argon, as the pathway of the electrical arc. Figure 6 shows a schematic representation of arc melting.

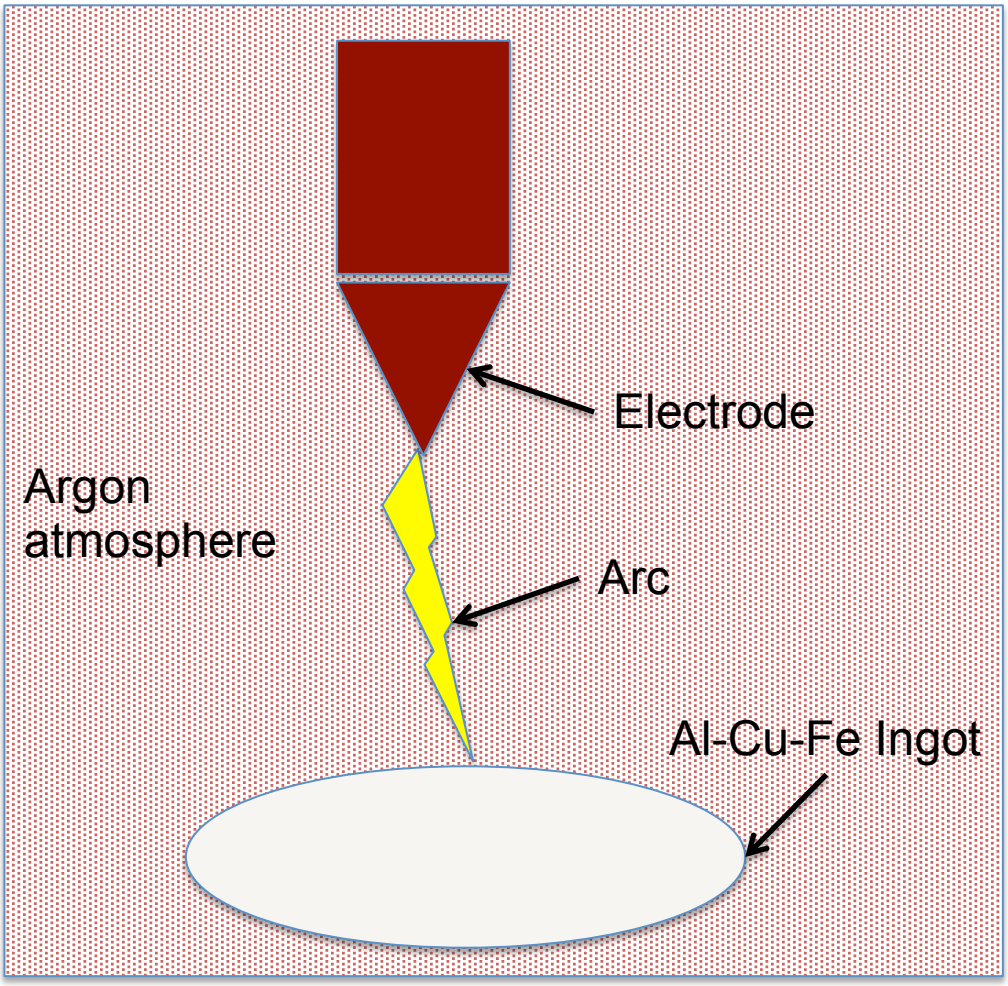

Figure 6. Arc melting schematic representation

3.1.1.1 Arc Melting Process

The alloys in these experiments were synthesized using an Edmund Buhler GmbH Arc Melter (Dr. Ibrahim Karaman's lab, Texas A&M University,Mechanical Engineering). A challenge that continued to present itself throughout the preparation of the material samples was in the presence of oxidation. If the base materials were not properly etched in advance, the final product's composition could vary significantly,

from melt to melt. Additionally, excess oxidation in the materials led to noticeably increased porosity in the samples, which could affect the quality of hardness and tribological data. Thus, it was imperative that each sample be thoroughly etched in an appropriate chemical bath to remove oxides. In the case of the iron, a nital etchant (95% ethanol, 5% nitric acid by volume) was used to remove iron oxide. A Keller's etchant (95% distilled water, 2.5% nitric acid, 1.5% hydrochloric acid, 1% hydrofluoric acid) was used to remove the layer of aluminum oxide surrounding the aluminum pieces. Copper did not require an etchant, as it had no noticeable presence of oxidation. Once etched, the materials were dried and weighed for the appropriate alloy composition. In each instance, a small amount of excess aluminum was used to compensate for the rapid formation of oxidized aluminum around the outside of the sample. The chamber of the arc melter was thoroughly cleaned to avoid any possible contamination from excess particles, such as carbon. The sample was placed in the copper crucible of the arc melter, and the chamber was bolted shut. The samples were layered according to their sublimation pressures, with the material having the lowest sublimation pressure placed on the bottom. This was done to minimize the likelihood of losing materials in a gaseous form, if temperatures were to become too high. At this point, the chamber was vacuumed by a series of pumps to remove any air present. The chamber was then filled with argon, in order to create a path for the arc to contact the sample from the electrode. The sample was melted to combine the materials into a single, adjusting the current as necessary (150 amps for 60-120 seconds). The sample was flipped and melted again approximately three to five times for each sample. This was done to ensure the

homogeneity of the sample and adequate melting of all materials present. Samples were solidified by a water-cooling system that passed underneath the crucible, which caused a rapid drop in the sample's temperature after each melt. The argon was finally removed from the chamber, and the chamber was opened to collect and inspect the samples.

3.1.2 Mechanical Pulverization of Alloys

In order to make a composite material, containing the Al-Cu-Fe quasicrystals within a UHMWPE matrix, the Al-Cu-Fe alloys needed to be in the form of powders. It was important that the powders be relatively small in size, so that sufficiently homogeneous mixing with UHMWPE powders would occur. In addition, smaller sized alloy powders would lessen the likelihood of large chunks of metal damaging the matrix during tribological testing, and results from these tests would likely be more consistent, if alloy powders were predominantly refined to nano-scale size.

The Al-Cu-Fe ingots were crushed to smaller pieces with the use of a gear-driven mechanical press. The ingots were placed between two steel plates, as the machine's arm that drives the mechanical motion was rotated. Due to the hard, brittle nature of the ingots, a modest amount of pressure from the machine initiated pulverization. Once the ingots were crushed into small, micro-scale pieces, further crushing was done with the use of a mortar and pestle. These were cleaned before use, to minimize contamination of the powders. The pieces were continually ground with the mortar and pestle, until a fine, nano-scale powder was formed. Figure 7 shows the devices used to crush the Al-Cu-Fe ingots and form their powders.

Figure 7. Mechanical press (left) and mortar and pestle (right)

3.1.3 Compression Molding (UHMWPE Processing)

Several techniques are available for the processing of UHMWPE, including sintering powders, injection molding, and compression molding. Each poses advantages and disadvantages, and each process will be related to particular uses of the end product.

In the case of sintering plastic powders, this processing method allows the development of highly porous plastics. This may be practical in applications requiring filtration, or in instances of controlling fluid flows. However, a low porosity polymer is of interest in the present research, so this method would be impractical.

Injection molding works by heating and melting polymeric powders, then pressing the viscous, flowing polymer through a die. This processing method is used in many manufacturing processes, but it is not of interest for this research. This is due to the concern with metallic powders collecting into clumps, as it is extruded through the

die. In addition, it is particularly difficult for UHMWPE to flow through a die, as it has a very high viscosity.

Compression molding works by placing polymeric powders into a frame/die, between two heated plates. These plates will melt the polymer, while applying an external pressure to increase density of the final product. Due to the ease of this processing method, the lessened likelihood of metallic powders collecting during flow, and the reduced porosity of finished samples, compression molding was selected for the present research.

3.1.3.1 Compression Molding Process

The compression molder was set to a temperature of 180°C to ensure thorough melting of the polymeric powders and sufficient flow, without reaching a temperature that would lead to degradation of the polymer. Such a high temperature was necessary, as the polymeric powders had such a high melting point (~140°C) and viscosity, due to the high molecular weight. The powder was placed onto the heated plates, within a rectangular frame to maintain a uniform thickness and shape of the sample. Pressure was applied to the heated plates by a hydraulic piston (4 tons on a $3\frac{5}{8}$" diameter ram), and the samples were held for approximately 30 minutes to sufficiently melt. The pressure was then relieved, and the plates and sample were allowed to cool. The final product was easily removed, and not further preparation of these samples was necessary for testing purposes. Figure 8 shows the compression molder used in these tests, as well as an example of a finished UHMWPE-Al-Cu-Fe composite sample.

Figure 8. Compression molder (left) and UHMWPE-Al-Cu-Fe composite sample (right)

3.2 Sample Preparation for Testing

After synthesizing the materials of interest, it was necessary to prepare the samples for the materials characterization tests. In the case of the Al-Cu-Fe sample, the ingot had an irregular shape and needed to be cut into smaller cross sections of the material. As these slices were rather difficult to handle for polishing, they were baked into a polymer made by Buehler (PhenoCure/Bakelite) using a hot compression-mounting device, also made by Buehler. This allowed the sample to be easily handled when performing a mechanical polishing of the surface. The surface was then polished to a nano-scale roughness, using successively increasing grits of silicon carbide polishing pads (240, 320, 400, 600, 800, 1200). The final step, to achieve near-mirror finish, was the use of a felt-like polishing pad, with an alumina-based fluid for a thorough finish. The roughness of these samples will be described in the portion of this

paper related to Atomic Force Microscopy. For the polymeric and composite material samples, this mounting procedure was unnecessary, as the samples were larger and easier to handle. In addition, the temperature treatment of the mounting polymer may have led to changes in the physical properties of the UHMWPE.

3.3 Surface Morphology

3.3.1 Atomic Force Microscope (AFM)

3.3.1.1 Background

Atomic force microscopy (AFM) utilizes a micro-sized probe to produce 3D images of surfaces, with a sub-nanometer precision. The probe tip will be atomically fine, allowing it to be attracted and repulsed by the sample surface's atoms and generating a surface image with atomic resolution. AFM typically works by one of two operating modes. Contact mode is the first of these, where the tip is dragged along the surface of a sample. This works very similarly to a stylus profilometer, or a phonograph. While this mode is beneficial for mapping large portions of the sample's surface, it provides little information about the sample's physical properties and causes the tip to degrade more rapidly. The other common mode of operation is non-contact mode. In this mode, the tip interacts with the material surface by van der Waals forces, as the tip oscillates at an amplitude below 10 nm. This mode has the advantage of not wearing down the tip and providing a high-resolution image of the surface. Figure 9 shows a schematic representation of a typical AFM device.

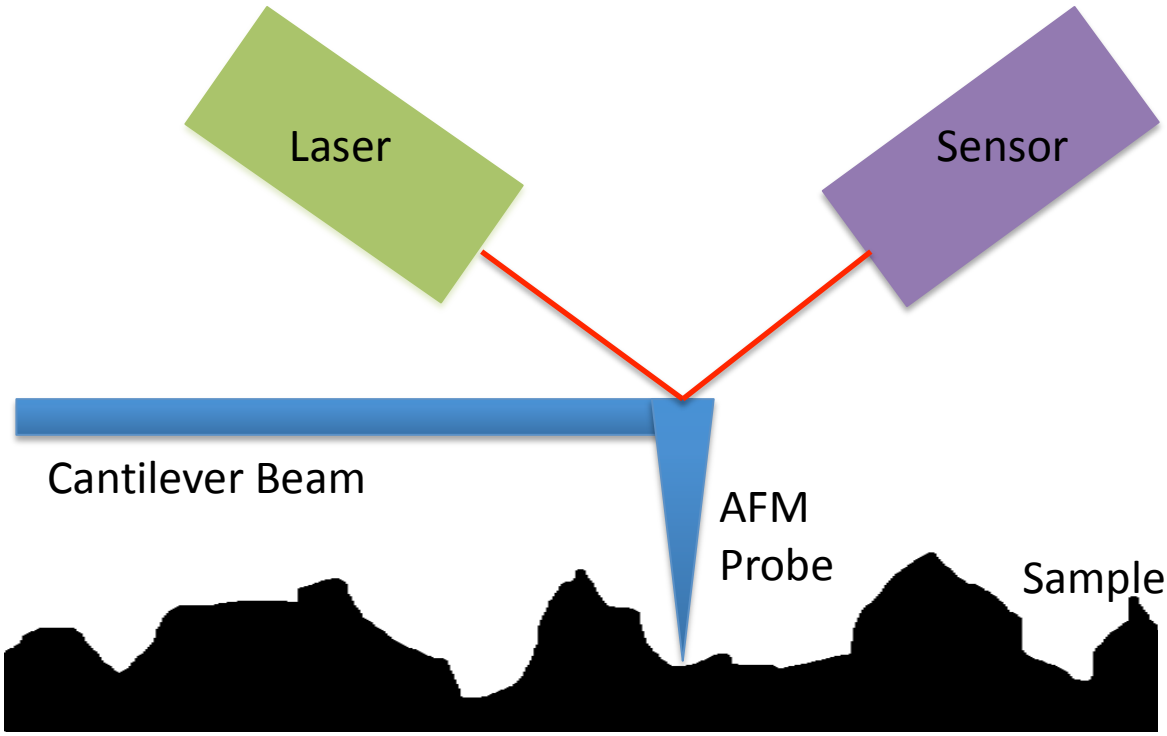

Figure 9. Schematic representation of AFM setup

3.3.1.2 Procedure

This research utilized the Pacific Nanotechnology Inc. Nano-R AFM (Dr. Hong Liang's Surface Science Lab, Texas A&M University, Mechanical Engineering). The samples were thoroughly polished by the method described in section 3.2. It was necessary that the sample, when placed onto the AFM scanner's surface, be flat, so it was ensured that the lower and upper faces of the sample were parallel. The machine, however, is able to compensate for some degree of imperfection in the perpendicularity between the sample and the imaging tool. Finally, AFM scans were completed using the non-contact mode.

3.4 Materials Characterization

3.4.1 X-Ray Diffraction

3.4.1.1 Background

X-Ray Diffraction, also known as XRD, is a commonly used material characterization technique that may be used to determine crystalline structures in a material by non-destructive examination. In addition to determining crystalline structures present in a material, the intensities of the peaks of the curve measured by the device may help determine composition of a material. Due to the presence of multiple phases in the Al-Cu-Fe alloy, the analysis of the XRD scan of the material will be focused to its dominant phases.

X-rays are electromagnetic waves, with high frequencies and short wavelengths. XRD works by monitoring the x-ray beams diffracted from a material's surface, as the result of coming into contact with a directed x-ray beam. The equation governing this analysis technique is Bragg's law, $2d \sin\theta = n\lambda$, where d describes the distance between diffracting planes, θ is the incident angle, n is an integer, and λ is the beam's wavelength. The source beam will cause the contacted particles to refract a small portion of its radiated intensity as a wave. When these waves interact constructively in directions where the difference in path-length ($2d \sin \theta$) is equivalent to an integer multiple of the wavelength ($n\lambda$), a portion of the source beam deflects by an angle 2θ. This 2θ angle is recorded to produce the XRD's plot.

A beam from an x-ray source is directed toward a stationary sample at a particular angle. As the beam comes into contact with the material sample's various

phases and crystalline structures, x-ray beams will be diffracted at different angles. A moving detector will sense these beams and transmit the data to a data acquisition system to collect and organize the data. The angles and intensities of these diffracted beams will correspond to particular crystalline structures. Based on literature material and simple calculations, a clearer picture may be attained of the sample's microstructure. It should be noted that, although XRD results should be consistent between polished, unpolished, and powder samples of the same material, results may vary from potential contamination and cold working effects of polishing a surface. Examples of XRD data may be seen in the results chapters of this paper. Figure 10 shows a schematic representation of an X-Ray Diffractometer.

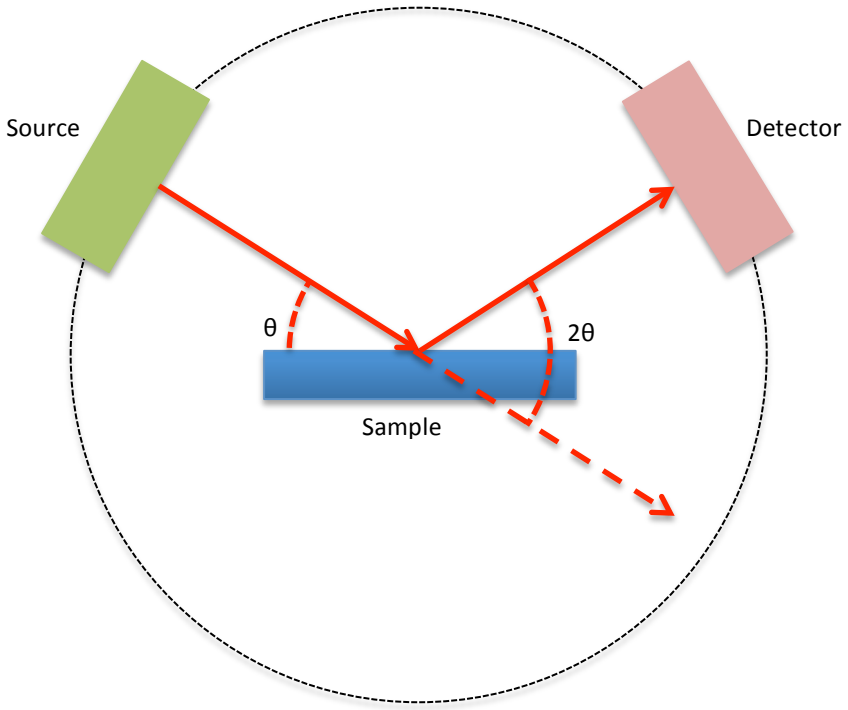

Figure 10. XRD schematic representation

3.4.1.2 Procedure

XRD scans were performed using a Bruker-AXS D8 Advanced Bragg-Brentano X-ray Powder Diffractometer (Texas A&M University, Chemistry). These scans were used to determine the phases present in an Al-Cu-Fe alloy, as well as the percentage of the alloy that each major phase constituted. The x-ray source was a copper emitter, and the machine utilized a 250 mm two-circle goniometer. Scans were taken between 20 and 80 degrees, and each scan took approximately 10 minutes, providing adequate resolution for evaluation purposes. The scans directed data to a program named EVA, which would create a .raw file. This file could be exported to a .txt file, then a Microsoft Excel file, to generate the final plots/figures. The XRD patterns generated were then compared to literature data and evaluated using the MDI Jade software to determine the identities of the peaks. This is discussed in more detail in the results chapters of this paper. The X-Ray Diffractomer used in this experiment may be seen in Figure 11.

Figure 11. Bruker D8 X-Ray Diffractometer

3.4.2 Electron Dispersive Spectroscopy-Scanning Electron Microscopy (EDS-SEM)

3.4.2.1 SEM Background

Scanning Electron Microscopy (SEM) is a microscopy technique that involves directing an electron beam onto a sample to collect an image, as a scanner collects the refracted electron beam. An electron gun will eject a beam of electrons, which are attracted toward an anode (positive charge) that is placed beneath an annulus-shaped cathode (negative charge). The repulsion and attraction interaction of these two electrodes with the electrons will direct the electrons toward a magnetic lens, which will condense the beam onto the sample. Upon interacting with the sample that is sitting on

the stage, some electrons will reflect onto a backscattered electron detector, while others will refract toward a secondary electron detector. The detectors will direct the collected data toward a data acquisition system, which will process and compile a final image and secondary data. This whole process takes place within a vacuum environment, in order to avoid interaction with gas molecules in the chamber and reduced image quality. A schematic representation of SEM is shown in Figure 12.

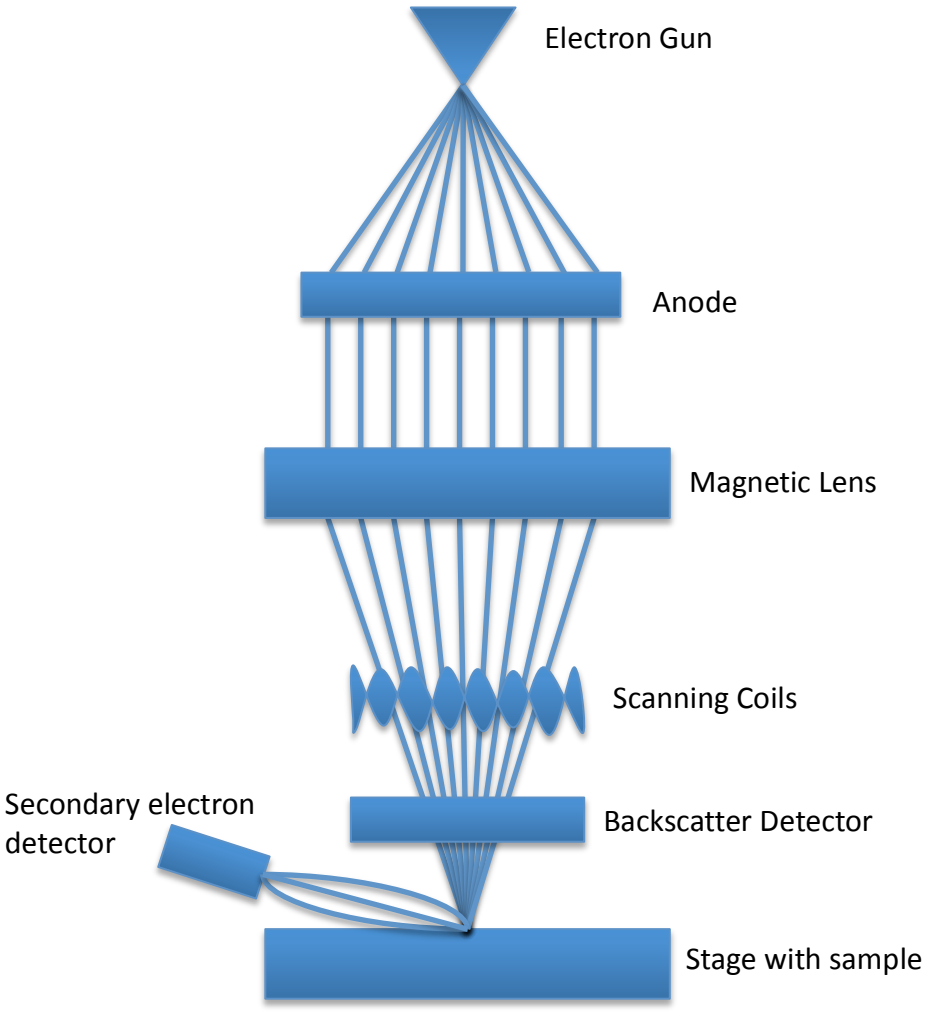

Figure 12. Schematic representation of SEM

Resolution of SEM images are typically on the scale of 1-20 nm, and the resolution is dependent upon electron wavelength, how extensively the electron beam will interact with the analyzed materials, and the magnetic lenses used to direct the electron beam. Though SEM does not inherently create three-dimensional images, it can be used with other tools and methods to construct these images.

3.4.2.2 EDS Background

Energy Dispersive X-Ray Spectroscopy (EDS) is an analytical technique utilized for evaluating the distribution of elements in a material and determining its chemical composition. This works by directing an excitation source (electron beam in the case of SEM) toward a sample. The beam will excite electrons in inner shells, causing them to be ejected. The vacancy of this electron will force an electron from an outer shell to fill the vacancy, creating an energy release in the form of an x-ray. The emitted x-ray will correspond to an energy signature, characteristic of a particular element, which may be recorded and interpreted to determine the elemental composition of the sample.

3.4.2.3 SEM-EDS Procedure

This research utilized the FEI Quanta 600 FE-SEM (Microscopy and Imaging Center, Texas A&M University). It was equipped with an Oxford EDS system, which includes a Silicon Drift Detector (SDD) and the software used to analyze the data collected from the detector. This device used a field emission electron gun, which results in higher resolution images and more accurate data, and a 20 kV voltage was

applied to excite the electron gun. Magnifications of 200-300x were used to evaluate an area of each sample large enough to see all phases present. EDS scans were directed toward determining the presence of Al, Cu, and Fe, the primary elements of concern. Each scan took approximately 50 seconds to complete.

3.5 Hardness

3.5.1 Microhardness Tester

3.5.1.1 Background

Hardness testing is a means of quantifying a material's resistance to plastic deformation, or its hardness. Although many hardness scales and tests exist, including Rockwell, Brinell, and Knoop tests, Vickers hardness testing was selected for this research. This is due to the broad range of hardness values the scale is capable of evaluating and the fact that it can be used for all metals, since the indenter is made of diamond and will be harder than any metal used. Microhardness indenting is practical for use in certain tests, where the material is especially brittle and could fracture under high loads, like those used in marcohardness testing. In addition, they can be used to identify microscopic variations in hardness.

Vickers hardness testing works by a relatively simple manner. A diamond indenter, whose sides will have a 72° angle from the horizontal sample surface, is pressed against the surface of a material with a specified load. The surface area of the indention is then measured with a turret, containing the controls for an optical microscope and measuring lines. The applied load is divided by the surface area and

multiplied by a scale factor to provide a hardness value. Equation x shows the Vickers microhardness equation, where d is the average diagonal length in millimeters and L is the load in grams force. Figure 13 shows a schematic of the Vickers hardness test.

$$HV = 0.0018544 \times \frac{L}{d^2} \qquad \text{Eq. 3}$$

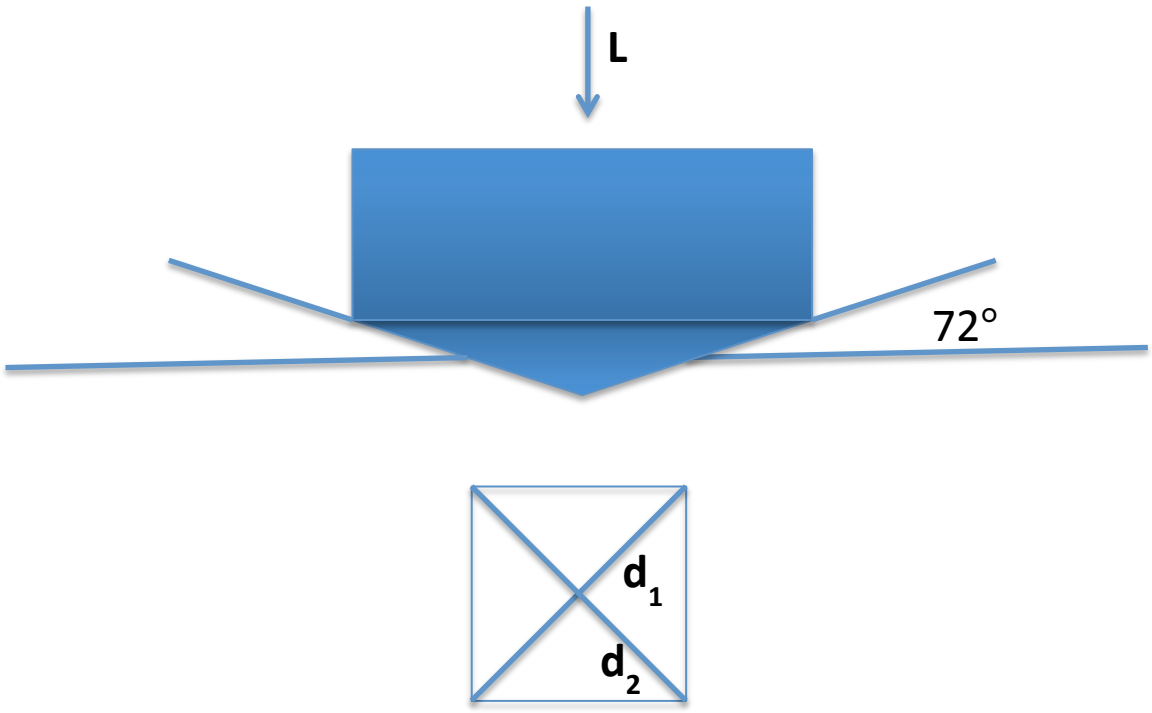

Figure 13. Vickers hardness test schematic

3.5.1.2 Procedure

This research utilized the Leco LM 300 Series Vickers Microhardness Indenter (Dr. Xinghang Zhang's lab, Texas A&M University, Mechanical Engineering). Tests were performed with a 300 gf load and a diamond Vickers indenter. The previously described polishing process was used to prepare the samples. For each alloy,

approximately 10 hardness values were collected to reduce uncertainty and get a more reliable value of hardness for the samples. A clear, flat area would be found, while looking at the sample with the indenter's microscope. The "Start" button would then be pressed, whereupon the indenter would slowly be pressed into the selected area. After the indentation was made, the turret would be used to align the photoetched measuring lines with the sides of the indentation mark. Once these were set, a hardness value would be generated. Figure 14 shows an image of the microhardness indenter used in these tests.

Figure 14. Leco LM 300 Series Vickers Microhardness Indenter

3.6 Wear Analysis

3.6.1 Tribometer

3.6.1.1 Background

In the setup of a tribometer, a sphere is loaded onto a test sample, along with a mass, to apply a precise force. This mass and sphere rest at the end of stiff lever, along with a frictionless force transducer. A linear tribometer, which is used in the research discussed in this paper, will simulate the reciprocation motion characteristic of many mechanisms encountered in daily life. A coefficient of friction for both forward and backward motion will be measured to provide cyclical data and simulate the operating life of a sample. The test will continue to run, until a particular coefficient of friction value is reached, or a particular number of cycles have been completed. It should be noted that, if necessary, the experimental parameters might be modified to allow testing under different conditions (e.g. humidity, temperature, lubrication, speed, contact pressure, time). A representation of a linear tribometer may be seen in Figure 15.

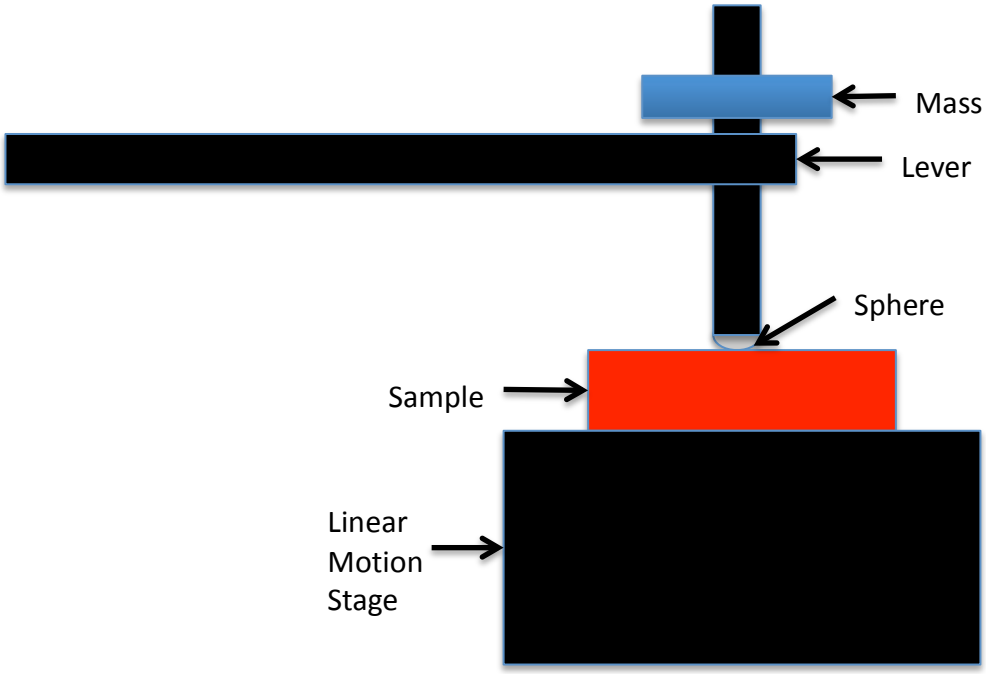

Figure 15. Linear tribometer schematic representation

A series of data types may be collected from the tribometer. Friction coefficient may be drawn from determining the deflection of the lever arm. The volume of material lost during the test can give the wear coefficient of a particular sphere-on-material setup. With the linear tribometer, in particular, the reciprocating motion of the tribometer provides insight into the variation of the static coefficient of friction over time. This is different from the pin-on-disk method, which will provide the dynamic coefficient of friction. Various tribometry tests may be applied to evaluate the performance of a material under different parameters and conditions. In the case of the present research, it was of particular interest to observe the linear tribological behavior of the materials, as this would be the most likely wear mechanism in a coating, or a joint replacement.

3.6.1.2 Procedure

This research utilized the CSM Instruments Linear Tribometer (Dr. Hong Liang's Surface Science Lab, Texas A&M University, Mechanical Engineering). Before attaching the sample to the linearly reciprocating stage, the stage's half-amplitude of motion was manually set to 1mm. First and foremost, the sample must be polished, with a relatively low surface roughness. This is done in order to minimize the effects of an irregular surface geometry on tribology results. In addition, this would minimize the likelihood of surface debris from accumulating at the beginning of the test. The sample was placed between two grips to ensure slipping would not occur, as this would certainly lead to significant data errors. The tribometer's lever was leveled, and the pin and sphere at the end of the lever were tightened in place, so that the applied force from the mass would be properly distributed to the sample. On the end of the lever, with its center of gravity directly above the sphere, a 5 N mass was set. The test was run at a linear speed of 0.9 cm/s in ambient air. The half amplitude of the stage's motion was set to 1 mm, and the total distance of the test was set to 10 m. The test was set to collect data on the friction coefficient of the test. The results of this test are described in more detail in the results chapters of this paper.

3.6.2 Profilometer

3.6.2.1 Background

Profilometry is a laboratory technique used to analyze the surface profile of a solid material, with a focus on characterizing and quantifying its roughness. The tools used to achieve this analysis are called profilometers, and there are several varieties of profilometers. They may differ in the physics used to analyze the surface, as well as whether or not direct physical contact is used to create a profile of the surface. In addition, some may only analyze a two-dimensional profile, whereas others may analyze a three-dimensional profile. The primary difference, nonetheless, is between contact and non-contact profilometers.

In the case of contact profilometers, a stylus resting at the end of a lever is dragged along the surface of a sample. A transducer will detect the vertical deflection of the stylus, as the stylus moves horizontally, and the transducer will transmit the data to a data acquisition system to record. This recorded data will show the height profile, or surface roughness, of the sample. Several parameters will dictate the quality and resolution of the data. The resolution of a sample's height profile will be impacted by the size of the stylus's tip, scan speed, and sampling rate of the data.

Non-contact profilometers, on the other hand, gather surface roughness data by optical scans of a sample's surface. Since the speed of this scan type is dependent on the speed of light being emitted and reflected, it tends to be a more rapid testing method for small sample areas and a preferred method of gathering surface roughness data. In

addition, the device is less prone to damage from repeated use, as it does not make contact with the sample and does not experience fatigue stress from repeated use.

3.6.2.2 Procedure

This research utilized the Zygo NewView 600 3D Profilometer (Dr. Hong Liang's Surface Science Lab,Texas A&M University, Mechanical Engineering). As the background of this analysis technique explains, optical profilometers are beneficial for their rapid scanning speed, resolution, and practicality for small areas of analysis. The scars from wear tests performed on the surfaces of the samples were approximately 2 mm long a few hundred microns wide. An optical, 3D profilometer was selected for this research. The sample was placed on a stage, which could be adjusted in three dimensions to get a level surface for imaging. This would allow the user to set an appropriate relative height for the surface roughness/profile measurements. As part of leveling the sample, a series of scans were performed to guarantee a symmetric surface profile, where the centerline of the wear test was shown to be the lowest point. It was necessary that the entire width of the wear scar would be visible in the scans. So, adjusting the sample's level was necessary for this, as well. Once leveling was complete, the image could be taken and used for analysis of the wear profile and wear rate. The results of these tests are described in more detail in the results chapters of this thesis. Figure 16 shows the 3D profilometer used for these experiments.

Figure 16. Zygo NewView 600 3D Profilometer of Surface Science Lab at TAMU

CHAPTER IV

MATERIAL PROPERTIES AND TRIBOLOGICAL BEHAVIOR OF QUASICRYSTALS

This chapter presents and discusses the results from the synthesis of Al-Cu-Fe alloys and the analysis of these materials' properties.

The morphology of the Al-Cu-Fe alloys was first investigated. This was done through the use of Atomic Force Miscroscopy (AFM) to observe surface roughness.

Next, the crystallography and composition of the alloys were investigated. X-Ray Diffraction (XRD) was used to determine phases present in the alloys. To observe the distribution of elements and phases across the surfaces of the alloys, Scanning Electron Microscopy-Electron Dispersive Spectroscopy (SEM-EDS) was used, as well as to verify the chemical composition of the samples.

Once materials characterization was complete, hardness data of the alloys was collected, which would be used for comparison with tribological results. Vickers microhardness was used for all experiments.

Finally, data was collected for the coefficient of friction and wear rate of the alloys. In addition, optical microscopy images were used to determine wear mechanisms of the alloys and composites.

4.1 Morphology

4.1.1 Arc Melted Ingot

After repeatedly arc melting each sample for improved homogeneity, the samples were solidified by a water-cooling system, which ran beneath the copper crucible in the arc melter's chamber. The drastic temperature difference between the water and the melted ingot led to a rapid solidification of the material. As a result, some prepared ingots experienced thermal shock, the accumulation of internal stress by one part of an object expanding/contracting at a different rate than another part of the object. In this case, the material's brittle nature, in some instances, would cause a sudden fracture of the material. However, this did not occur in most of the prepared ingots. Figure 17 shows images of an Al-Cu-Fe alloy ingot after arc melting, where the effects of thermal shock are not visible (right), and another image is shown, where the effects of thermal shock may be seen (left).

Figure 17. Al-Cu-Fe alloy ingots after arc melting. Right sample fractured from thermal shock and highly brittle nature of material

4.1.2 AFM

As it was necessary to polish the surfaces of all samples before material characterization, hardness, and tribology testing, an AFM scan was conducted to examine the roughness of each polished sample. In order to reduce the effects of irregular surface geometry on error in analysis and testing, a nano-scale average surface roughness was desirable. The AFM scans evaluated an approximately 80 µm x 80 µm surface area and produced data for average roughness, root mean square roughness, and peak roughness values. The polished samples typically had an average surface roughness from 15 nm to 20 nm, and some large scratches were present on surfaces, though they were minimal in numbers. Figure 18 shows an AFM image collected from a polished Al-Cu-Fe sample.

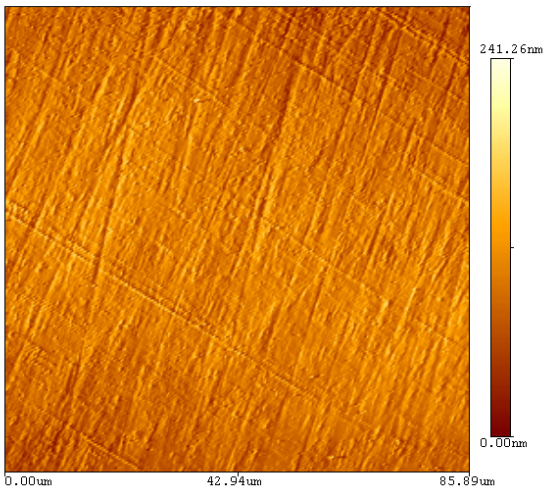

Figure 18. AFM image of hand-polished alloy sample

4.2 Crystallography and Composition

4.2.1 X-Ray Diffraction

Several XRD scans were conducted to determine the phases present in the three alloys. As was previously mentioned, all alloys were arc melted and rapidly cooled. In the case of the $Al_{65}Cu_{20}Fe_{15}$ alloy, a separate annealing process took place after the arc melting to increase the percentage of quasicrystalline phases present, with respect to the alloy's total composition. This was accomplished by heating the sample in an argon-atmosphere furnace at 600°C for 3 hours. Figures 19 shows the XRD results of $Al_{50}Cu_{20}Fe_{15}$. In addition, these figures are labeled with the observed phases present.

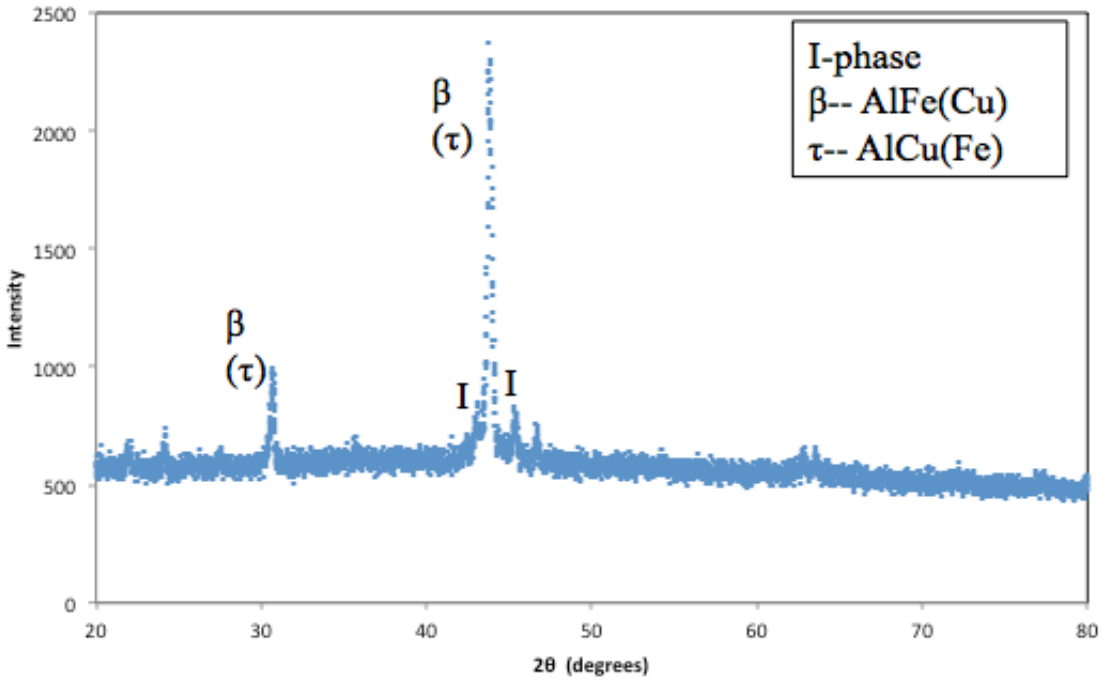

Figure 19. XRD results of $Al_{50}Cu_{20}Fe_{15}$

The XRD patterns produced from the scan of the $Al_{50}Cu_{20}Fe_{15}$ alloy showed several peaks present, though one peak showed the greatest intensity. Determining the composition of this peak, as well as those less dominant ones, was done by a combination of (1) searching relevant literature for corresponding peaks and (2) using software analysis to determine the corresponding phases of these peaks. Figure 20 shows results from the analysis of the XRD scans, using the MDI Jade software to determine the phases associated with peaks.

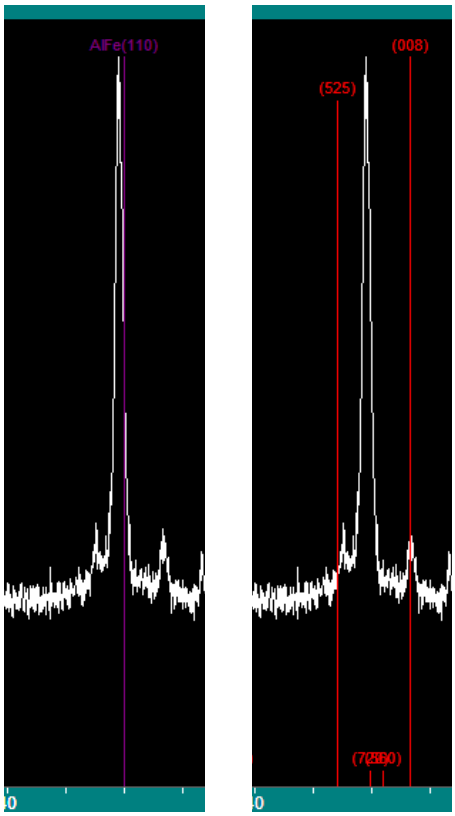

Figure 20. XRD analysis of $Al_{50}Cu_{20}Fe_{15}$ alloy showing (110) plane of β(τ) phase (Left) and quasicrystalline phase (Right)

From the investigation of literature related to the research of Al-Cu-Fe alloys, it was determined that the dominant peaks, centered at a 2θ value of 43.8°, was that of the β(τ)-AlFe(Cu)/AlCu(Fe) phase. The peak with the second highest observed intensity is also indicative of the β(τ) phase. The β(τ) phase is characterized by a CsCl structure. The small peaks to the left and right of the more intense β(τ) phase are those of an icosahedral quasicrystal phase. However, they have weak intensities, as they constitute less than 10% of the total composition. Thus, the physical behavior and properties associated with this material will be primarily a reflection of the characteristics associated with the β(τ) phase. Figure 21 shows a representation of the CsCl structure, as well as a depiction of the icosahedral quasicrystalline structure.

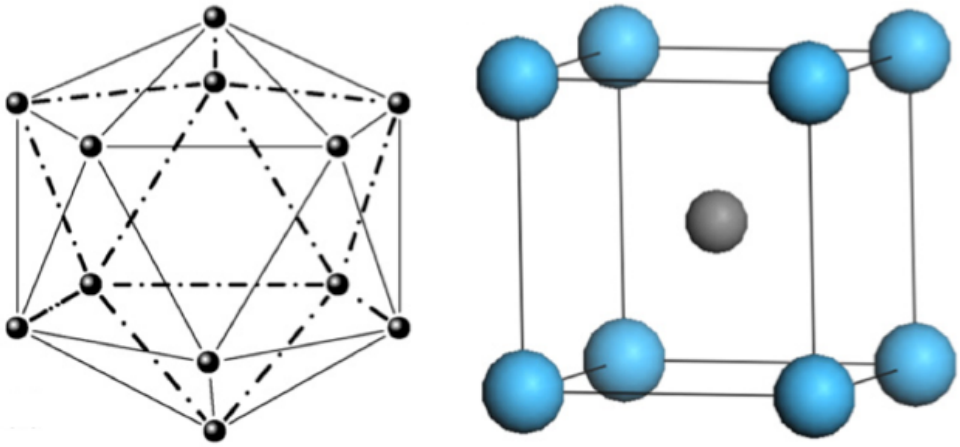

Figure 21. CsCl crystalline structure (left) and iscosahedral QC structure (right) [19, 54]

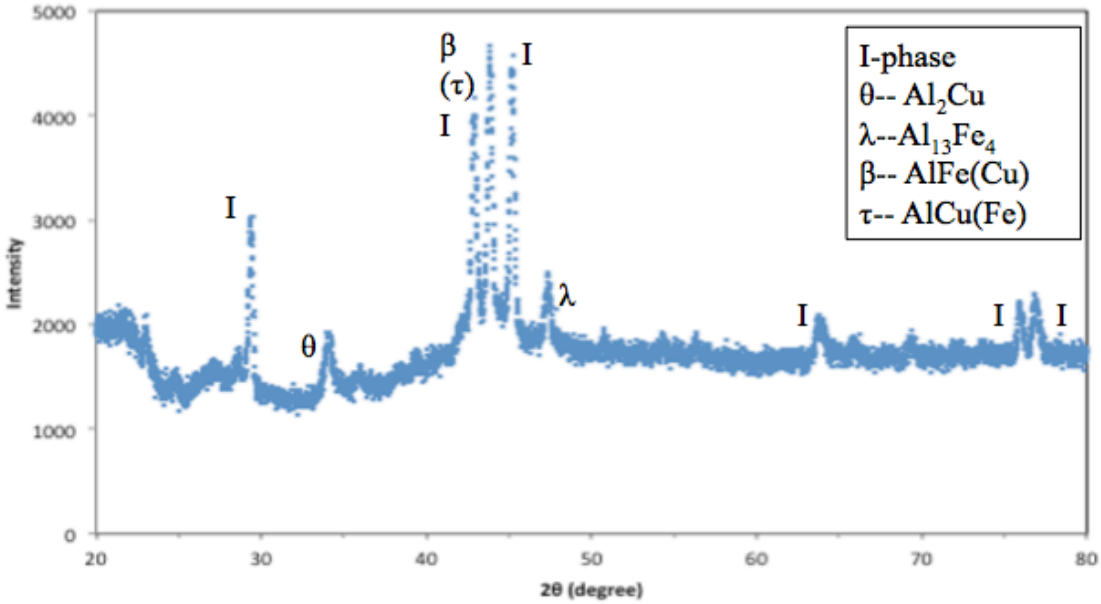

Figure 22. XRD results of un-annealed $Al_{65}Cu_{20}Fe_{15}$

Figures 22 shows the XRD results of un-annealed $Al_{65}Cu_{20}Fe_{15}$. The XRD patterns produced from the scan of the un-annealed $Al_{65}Cu_{20}Fe_{15}$ alloy showed several peaks present, though three peaks showed the greatest intensities. Once again, it was determined from the literature search that the middle of the three dominant peaks, centered at a 2θ value of 43.8°, was that of the β(τ) phase seen in the $Al_{50}Cu_{20}Fe_{15}$ alloy. The two other dominant peaks, to the left and right of the peak associated with the β(τ)-AlFe(Cu)/AlCu(Fe) phase, are the peaks of the icosahedral quasicrystal phase. By evaluating the XRD scans with the use of ImageJ image analysis software, it was determined that the icosahedral quasicrystalline phase accounted for 62.3% of the total structure of the material. In addition, a monoclinic λ-$Al_{13}Fe_4$ phase and a tetragonal θ-Al_2Cu phase were observed, though these phases accounted only for a minute portion of

the material's structure (< 5%). Figure 23 shows results from the analysis of this alloy's XRD scan, using the MDI Jade software to determine the phases present.

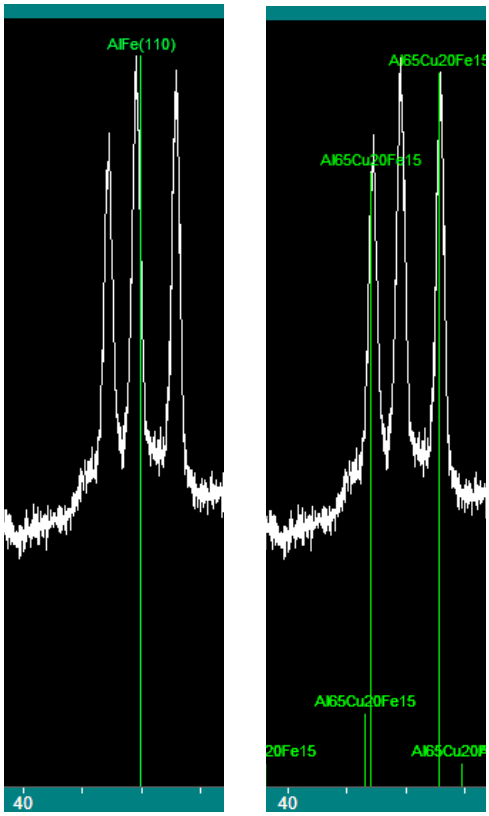

Figure 23. XRD analysis of un-annealed $Al_{65}Cu_{20}Fe_{15}$ alloy showing (110) plane of β(τ) phase (Left) and quasicrystalline phase (Right)

Figures 24 shows the XRD results of annealed $Al_{65}Cu_{20}Fe_{15}$. As in the case of the un-annealed $Al_{65}Cu_{20}Fe_{15}$ alloy, the annealed $Al_{65}Cu_{20}Fe_{15}$ alloy showed three dominant peaks. Once again, the middle of the three peaks was that of the β(τ)-AlFe(Cu)/AlCu(Fe) phase, and the two peaks to its side were indicative of the icosahedral quasicrystalline phase. For the annealed sample, though, the quasicrystalline

phase's intensity, relative to the β(τ) phase's intensity, has increased. Also, the presences of the monoclinic λ phase and the tetragonal θ phase have disappeared. As Figure 24 shows, the presence of the icosahedral quasicrystalline phase constitutes the vast majority of the material's structure (82.7%).

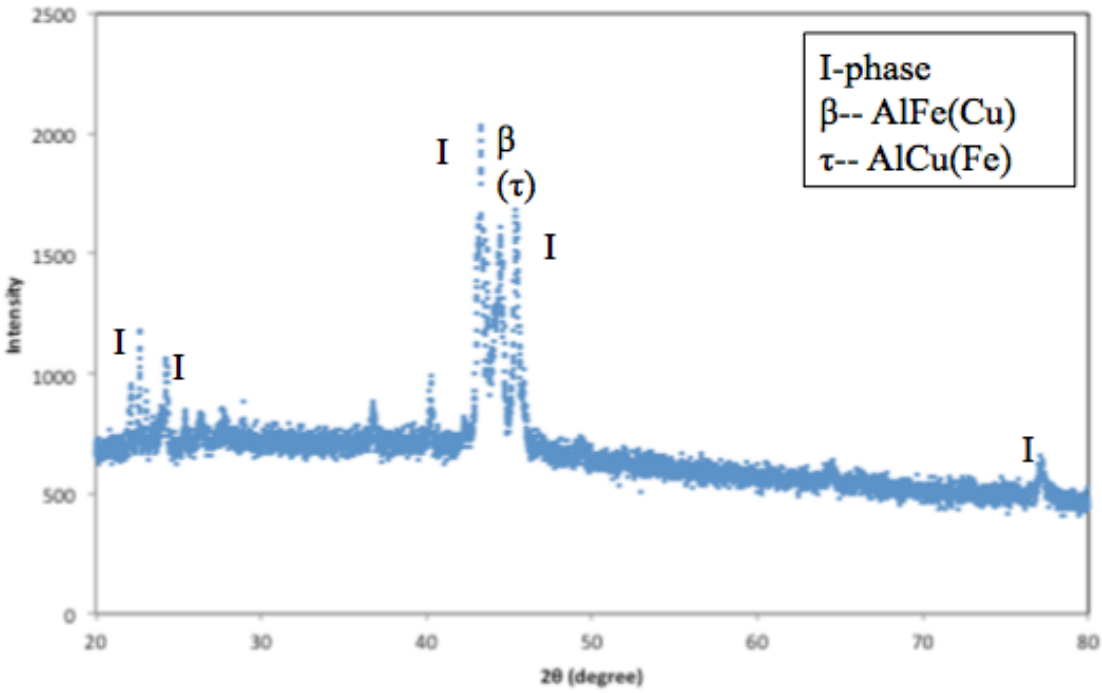

Figure 24. XRD results of annealed $Al_{65}Cu_{20}Fe_{15}$

From Figure 25, the analysis of the XRD results using the MDI Jade software may be seen. The image on the left shows the (110) peak of the β(τ) phase aligning with the material's centered large peak. The image on the right shows the icosahedral quasicrystalline peak aligning with the two outer large peaks.

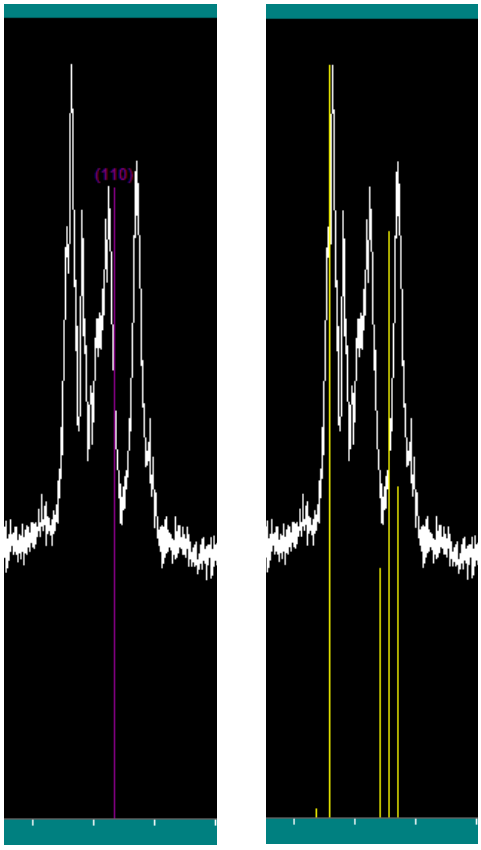

Figure 25. XRD analysis of annealed $Al_{65}Cu_{20}Fe_{15}$ alloy showing (110) plane of β(τ) phase (Left) and quasicrystalline phase (Right)

Thus, it is seen that annealing the $Al_{65}Cu_{20}Fe_{15}$ sample for 3 hours at 600°C led to an increase in the presence of the icosahedral quasicrystalline phase by 20.4%. While the un-annealed sample $Al_{65}Cu_{20}Fe_{15}$ sample has a large portion of both the quasicrystalline phase and the β(τ) phase present, the annealed $Al_{65}Cu_{20}Fe_{15}$ sample is overwhelmingly dominated by the icosahedral quasicrystalline phase. Contrary to this, the $Al_{50}Cu_{20}Fe_{15}$ sample was overwhelmingly dominated by the β(τ) phase.

4.2.2 SEM-EDS

A series of SEM images were collected to further evaluate the surface morphology of the samples. In conjunction with these images, EDS was used to map the distribution of elemental atoms across the alloys' surfaces and to determine the ratio of elements present in the samples. The distribution of three particular particles was investigated for each sample: aluminum (Al), copper, and iron. Although some particles, such as carbon (C), may have been present from contamination and polishing, they were neglected. As these images are intended to shed light on the change in composition, as a result of annealing, of the icosahedral-forming $Al_{65}Cu_{20}Fe_{15}$ samples, scans were not conducted on the $Al_{50}Cu_{20}Fe_{15}$ sample.

In the case of the un-annealed $Al_{65}Cu_{20}Fe_{15}$ sample, a very clear SEM image could be attained. This SEM image, as well as the elemental mapping images of Al, Cu, and Fe may be seen in Figure 26. The image showed the microstructure of the sample to be lamellar, as the phases of the material were thin and alternating, almost pearlitic. Aluminum was shown to be relatively evenly distributed throughout the sample, as it would appear in the icosahedral, $\beta(\tau)$, λ, and θ phases. It would be expected that Al would be less prevalent in the $\beta(\tau)$ phase, compared to the icosahedral phase, since Al accounts for less of the microstructure's composition. From this assumption, it may be concluded that the lighter portions of the SEM image are those of the $\beta(\tau)$ phase. In addition, this would explain why these same regions show more pronounced presences of Cu and Fe atoms, Fe being associated with the β phase and Cu with the τ phase.

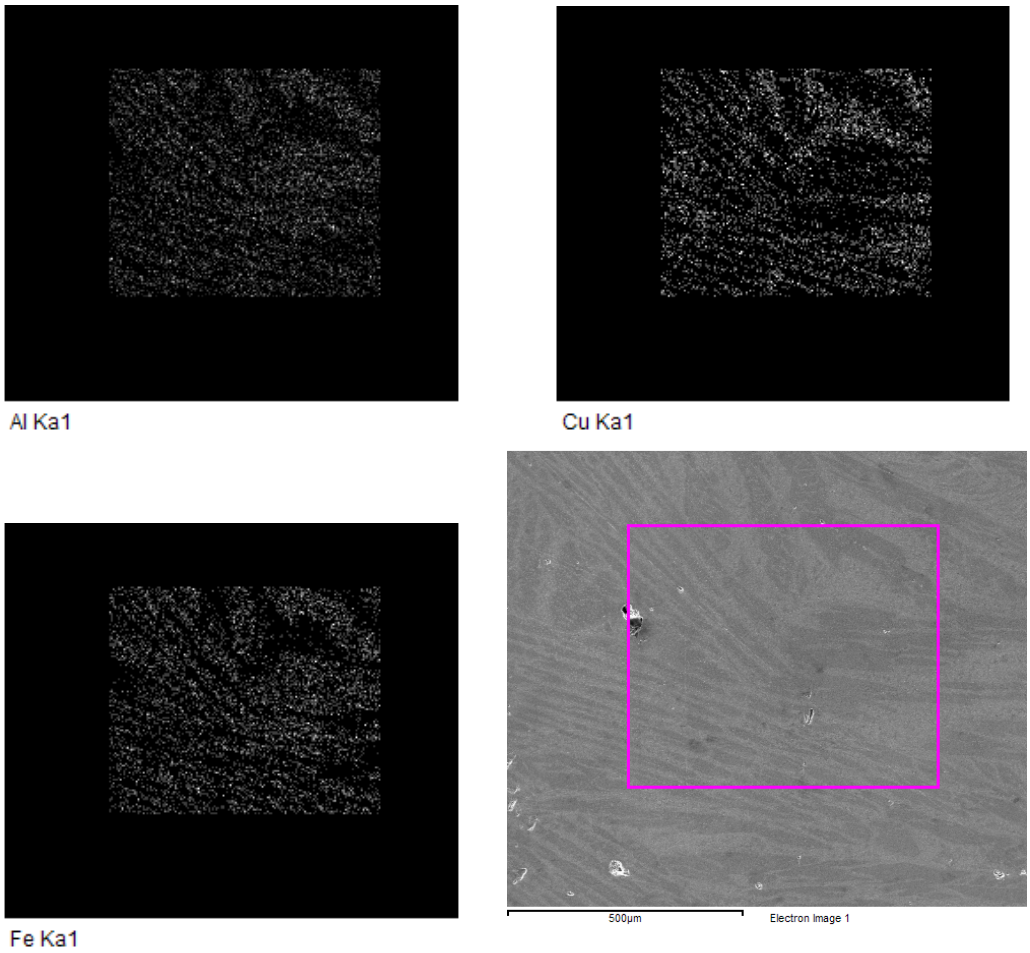

Figure 26. EDS mapping images of Al, Cu, and Fe atom distribution on surface of un-annealed $Al_{65}Cu_{20}Fe_{15}$ and SEM image of sample surface area evaluated

EDS analysis of elemental concentration was of interest, as there was a concern that oxidation of the aluminum would affect composition noticeably. This would allow the final composition of the alloy to be determined. The aluminum oxide layer formed at the outer surface of the melted sample, if sufficient etching was not performed, introduced a possibility of significantly altering the chemical composition of the remainder of the alloy.

The sample's composition was found by comparing the intensities of the elements. For the un-annealed $Al_{65}Cu_{20}Fe_{15}$ sample, this may be seen in Figure 27. In order of descending intensity and total atoms present, Al, Cu, and Fe were seen. Using the ImageJ image analysis software, the final composition of the sample was determined to be $Al_{62.5}Cu_{22.1}Fe_{15.4}$. This is statistically dissimilar from the expected $Al_{65}Cu_{20}Fe_{15}$ composition, as both are within the narrow range of compositions that would form an icosahedral quasicrystalline phase. Since the difference in composition is negligible for the purposes of this paper, the sample will continue to be referred to as having an $Al_{65}Cu_{20}Fe_{15}$ composition.

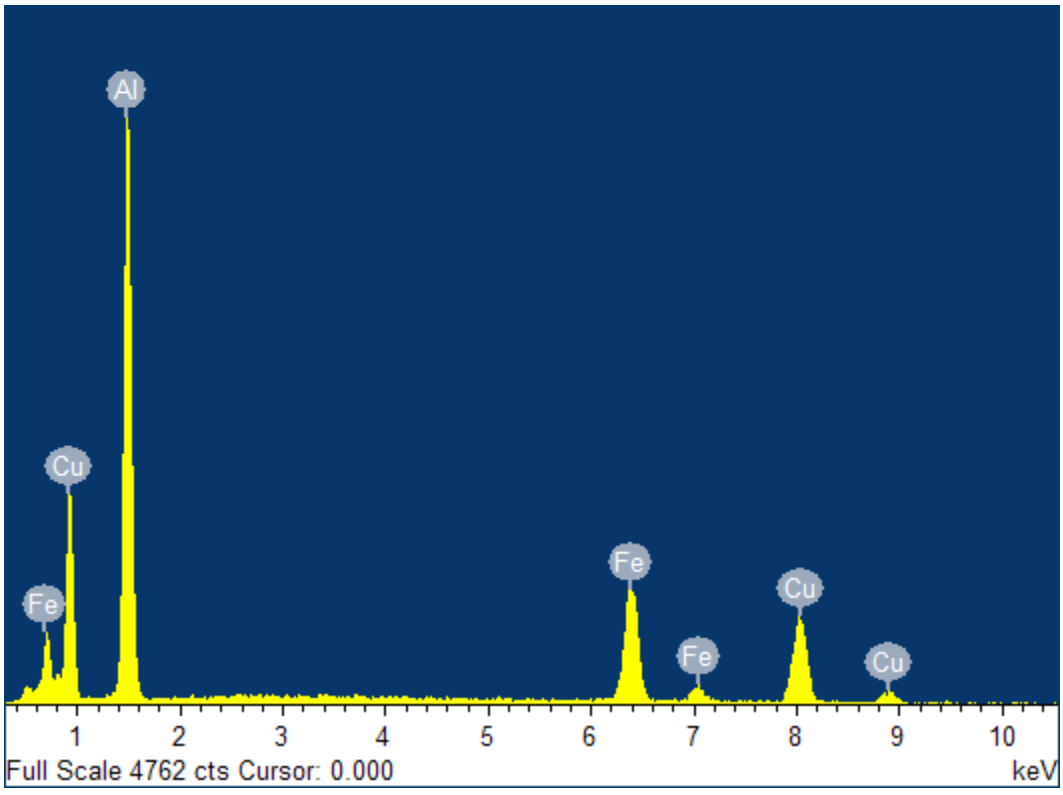

Figure 27. EDS analysis of elemental concentration in un-annealed $Al_{65}Cu_{20}Fe_{15}$

In the case of the annealed $Al_{65}Cu_{20}Fe_{15}$ sample, the SEM image did not show the microstructure of the samples as clearly. This SEM image, as well as the elemental mapping images of Al, Cu, and Fe may be seen in Figure 28. Each of the elements was more evenly distributed. This is a result of increased homogeneity and a predominantly icosahedral quasicrystalline structure, as the XRD tests from this sample suggested.

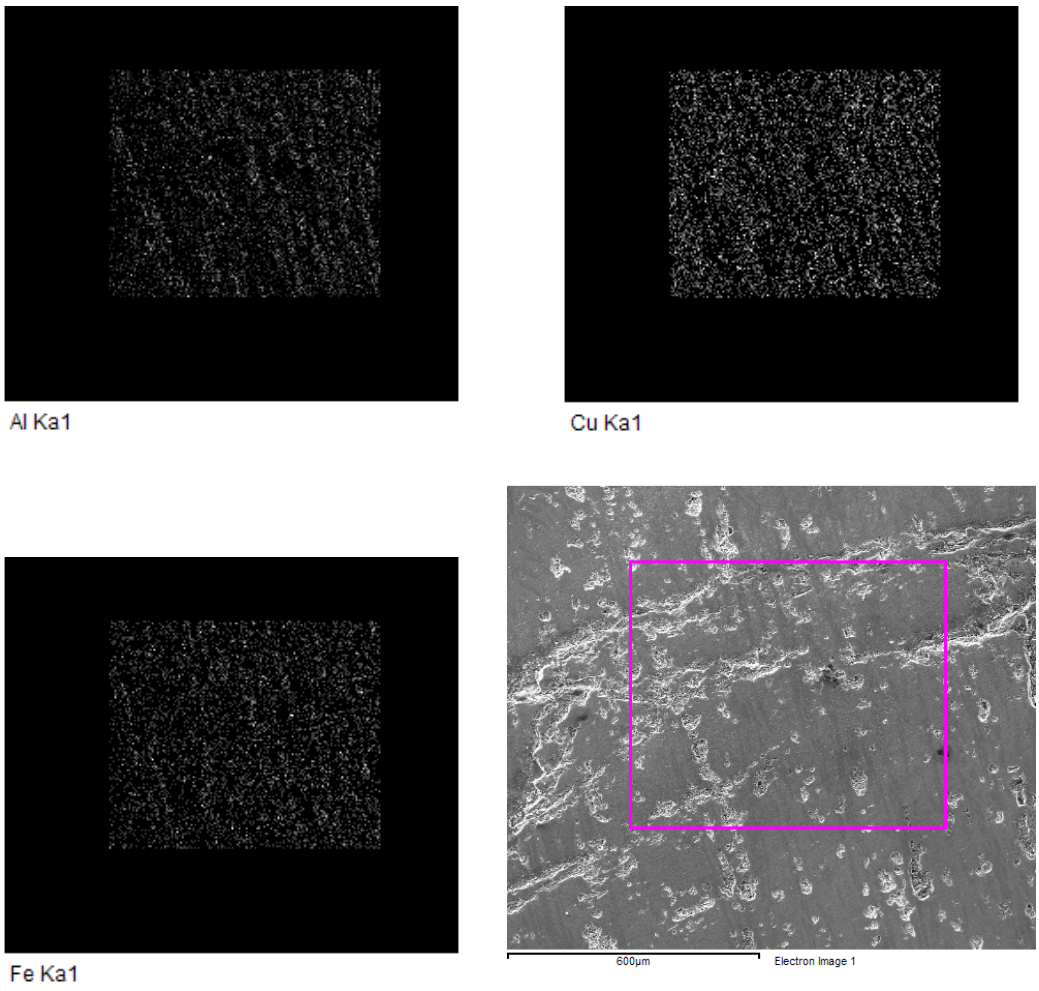

Figure 28. EDS mapping images of Al, Cu, and Fe atom distribution on surface of annealed $Al_{65}Cu_{20}Fe_{15}$ and SEM image of sample surface area evaluated

Using the ImageJ software to analyze the EDS scans for the annealed $Al_{65}Cu_{20}Fe_{15}$ sample, as shown in Figure 29, the composition of the alloy was determined to be $Al_{62.1}Cu_{21.1}Fe_{16.8}$. This is only slightly different from the composition of the un-annealed structure, so the same conclusion that the difference between actual and expected composition is negligible. The reduction in the Al & Cu content appears to be the direct result of the outward diffusion of these atoms.

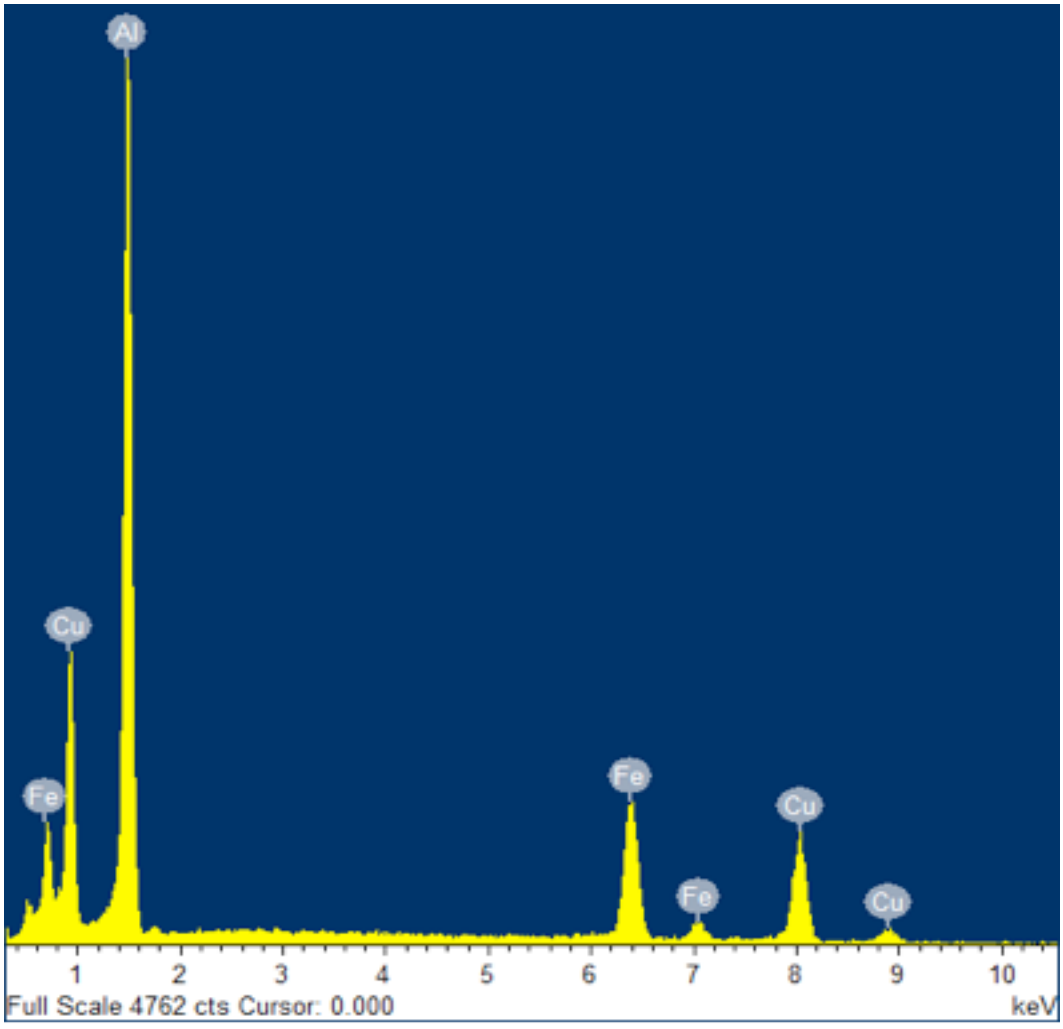

Figure 29. EDS analysis of elemental concentration in annealed $Al_{65}Cu_{20}Fe_{15}$

4.3 Hardness

Hardness data was collected for each of the three alloys investigated in this research. Measurements were taken across large areas of the samples, in order to guarantee an accurate depiction of the samples' hardness. This alleviated concern that hardness values were being recorded for a particular phase, or only at grain boundaries, as opposed to the entire sample. Still, the size of the indent was large enough that it was not of concern that only a single phase would be measured. The indent marks from the hardness tests of the annealed $Al_{65}Cu_{20}Fe_{15}$ sample may be seen in Figure 30. The brittle, hard nature of these materials is apparent in the formation of cracks at the corners of the indents.

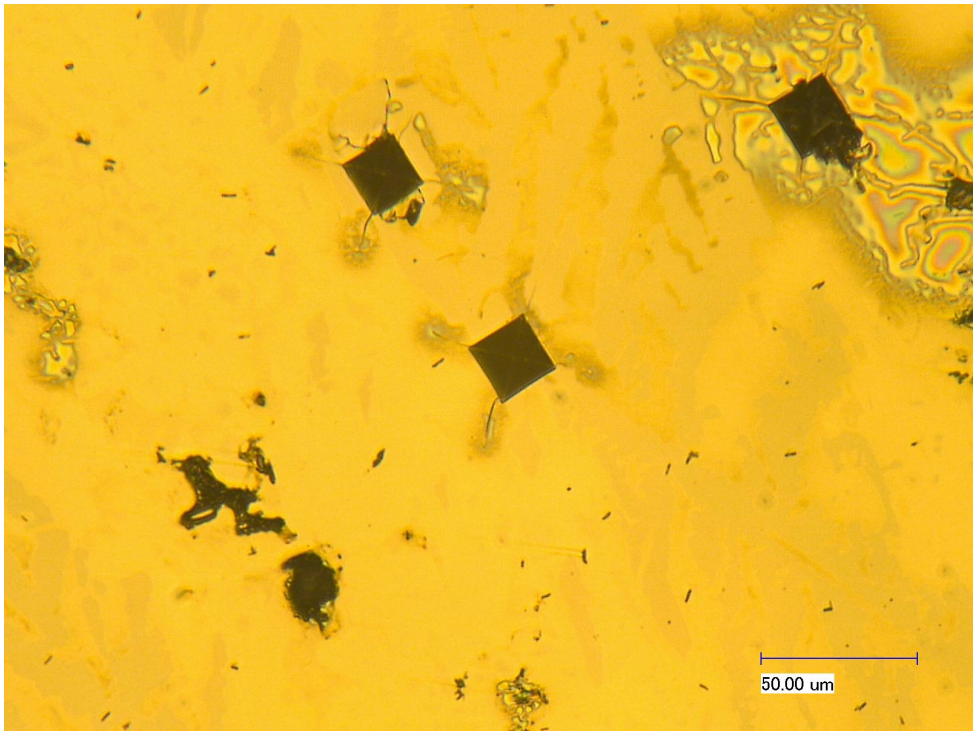

Figure 30. Hardness testing indents from annealed $Al_{65}Cu_{20}Fe_{15}$ sample

It was observed that the alloy exhibiting the greatest resistance to plastic deformation was the annealed $Al_{65}Cu_{20}Fe_{15}$, followed by the $Al_{50}Cu_{20}Fe_{15}$, and finally the un-annealed $Al_{65}Cu_{20}Fe_{15}$. The improved hardness of the annealed sample can logically be concluded to be the result of improved homogeneity of the sample, as the harder icosahedral quasicrystalline phase will dominate the behavior of the material, and less grain boundary interaction with the β(τ) phase will occur. Thus, it may be concluded that the icosahedral phase was the hardest phase present. The hardness results of the three alloys may be seen in Figure 31.

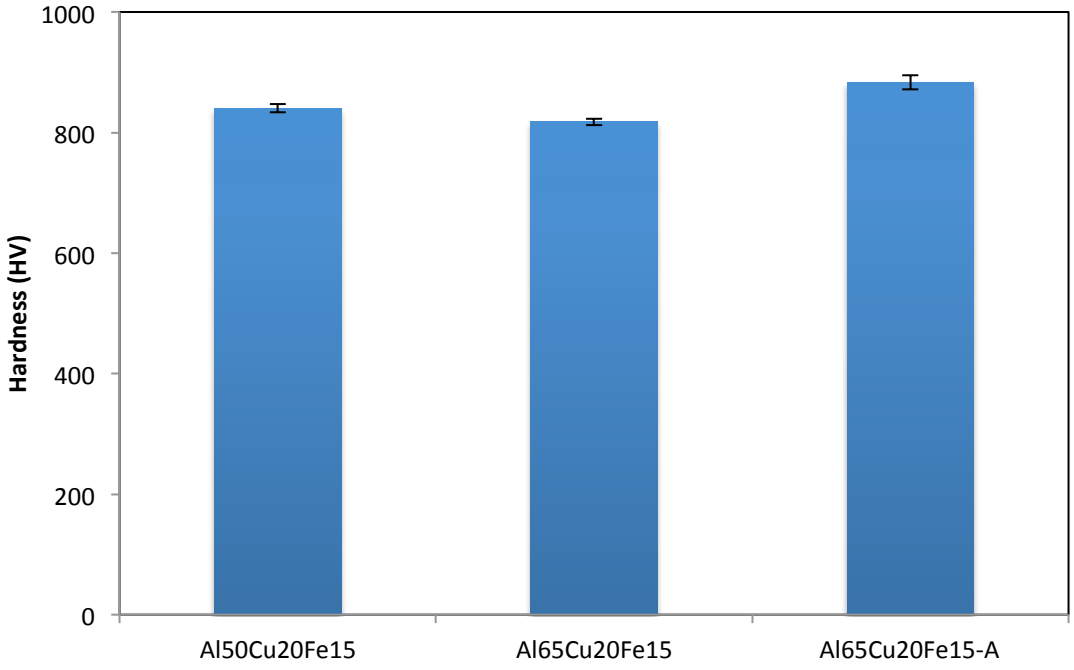

Figure 31. Vickers microhardness (HV) results of $Al_{50}Cu_{20}Fe_{15}$, un-annealed $Al_{65}Cu_{20}Fe_{15}$, and annealed $Al_{65}Cu_{20}Fe_{15}$ alloys

4.4 Tribological Performance

4.4.1 Frictional Behavior

Using the linear tribometer, a series of tests were conducted to evaluate the friction performance of each of the alloys. The material of the ball used for these tests was a stainless steel. A wear scar of 2mm length was generated, over the course of approximately 20,000 laps. From these tribometry tests, a series of plots were generated for the coefficients of friction for the samples. Examples of the plots for coefficient of friction of $Al_{50}Cu_{20}Fe_{15}$, un-annealed $Al_{65}Cu_{20}Fe_{15}$, and annealed $Al_{65}Cu_{20}Fe_{15}$ alloys, rubbing against a stainless steel ball, may be seen in Figure 32,

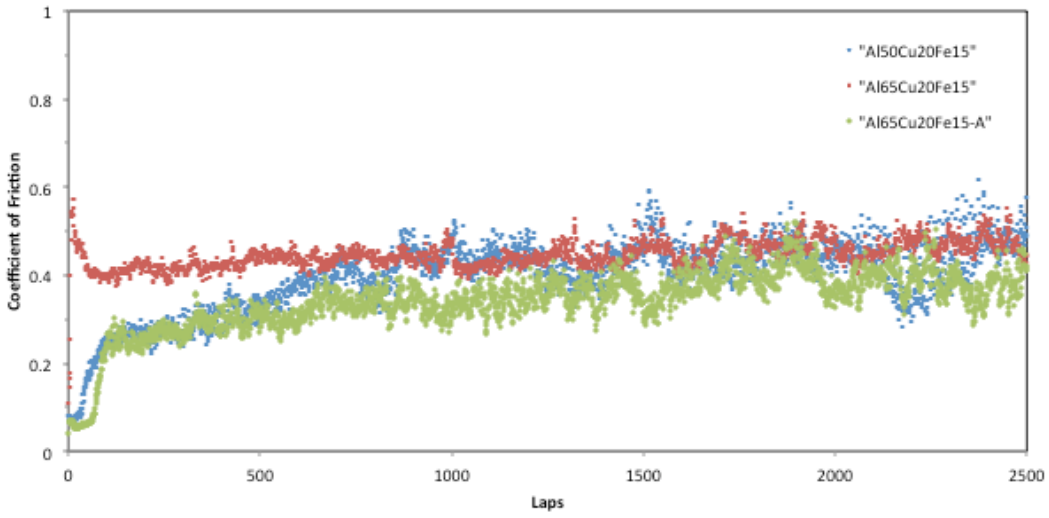

Figure 32. The coefficient of friction of $Al_{50}Cu_{20}Fe_{15}$, un-annealed $Al_{65}Cu_{20}Fe_{15}$, and annealed $Al_{65}Cu_{20}Fe_{15}$ alloys

Frictional behavior, from the tribometry tests, was characterized by an initially low, consistent coefficient of friction. This was followed by a sudden rise in the coefficient. After the coefficient continued to increase for a brief period, it would begin to level and maintain a consistent value. This may be seen as being the case in each of the three alloys. Additionally, the coefficient of friction values of all three alloys are relatively close, within a range of 0.6. The lowest of these was seen to be the value of the annealed $Al_{65}Cu_{20}Fe_{15}$, followed by the $Al_{50}Cu_{20}Fe_{15}$, and finally the un-annealed $Al_{65}Cu_{20}Fe_{15}$. The order of coefficient of friction values is similar to that of the inverse of hardness values, though the range of error in the coefficient of friction values makes their order more difficult to discern. The plot showing the average coefficients of friction values for all three samples, as well as uncertainty, may be seen in Figure 33.

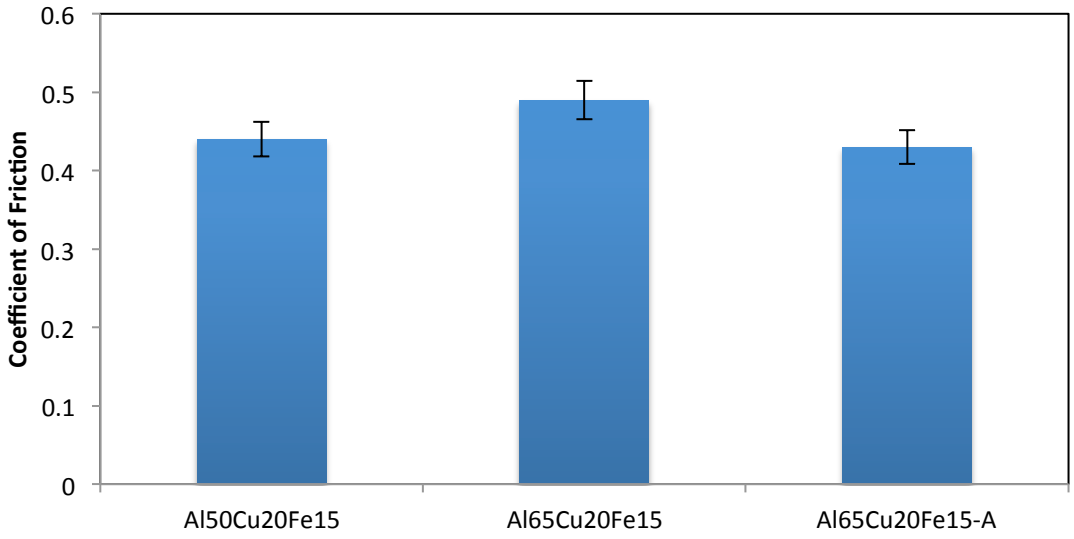

Figure 33. Coefficient of friction results of $Al_{50}Cu_{20}Fe_{15}$, un-annealed $Al_{65}Cu_{20}Fe_{15}$, and annealed $Al_{65}Cu_{20}Fe_{15}$ alloys

4.4.2 Wear Scar and Wear Track Morphology

Wear scars were created, as the result of the tribometry tests. These scars were used, with the aid of an optical profilometer/interferometer, to evaluate the volumes of material lost from the friction tests and the corresponding wear rates. Examples of the resulting profilometry images of $Al_{50}Cu_{20}Fe_{15}$, un-annealed $Al_{65}Cu_{20}Fe_{15}$, and annealed $Al_{65}Cu_{20}Fe_{15}$ alloys may be seen in Figures 34, 35, and 36, respectively.

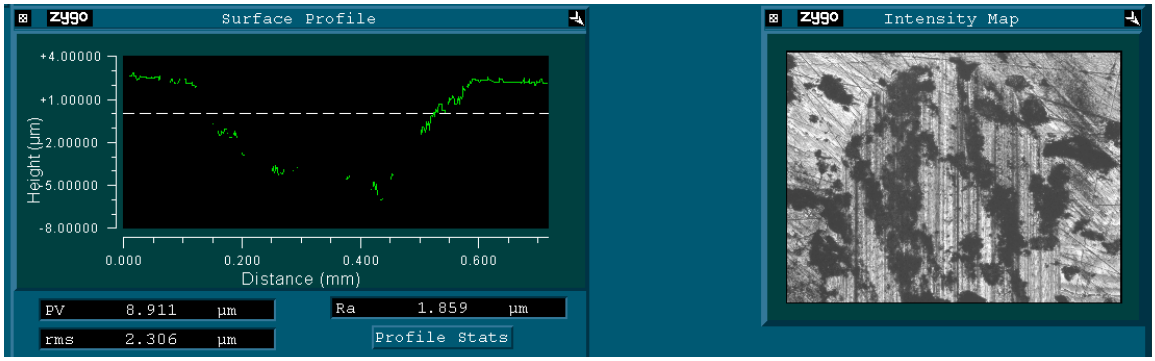

Figure 34. Profilometry of wear scar on $Al_{50}Cu_{20}Fe_{15}$ sample. PV: 8.911 µm

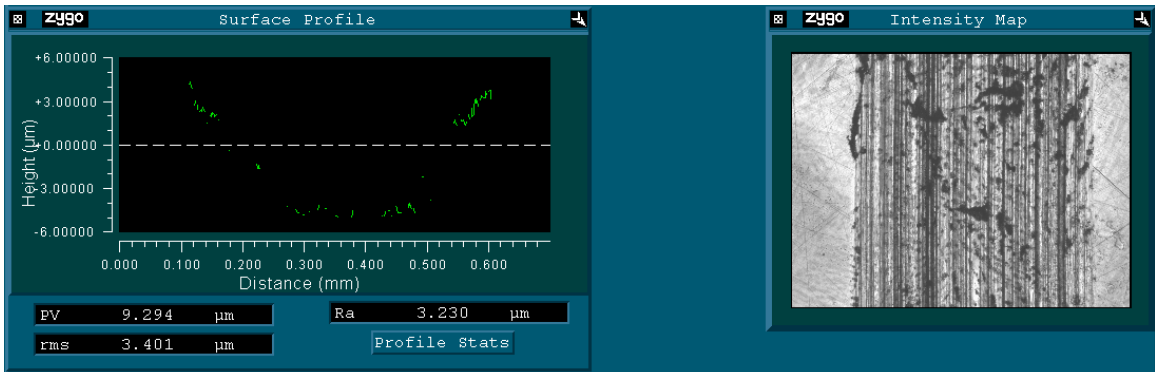

Figure 35. Profilometry of wear scar on un-annealed $Al_{65}Cu_{20}Fe_{15}$ sample. PV: 9.294 µm

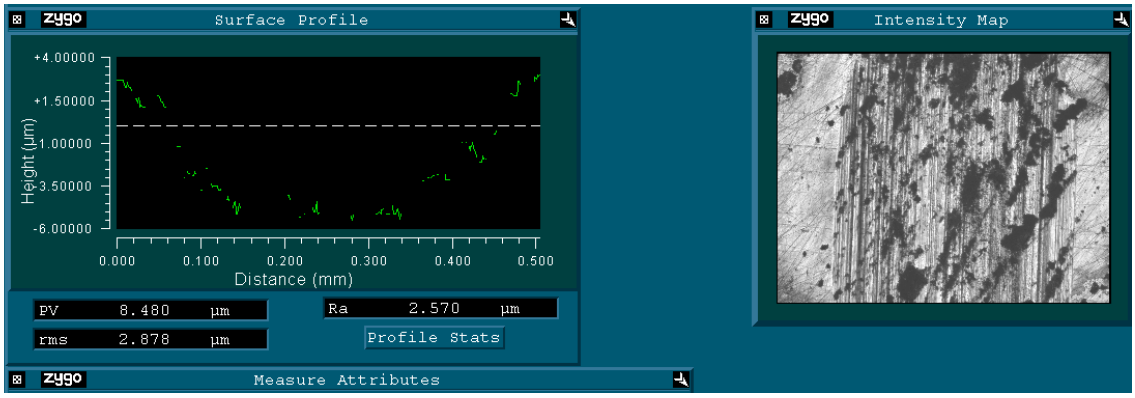

Figure 36. Profilometry of wear scar on annealed $Al_{65}Cu_{20}Fe_{15}$ sample. PV: 8.480 µm

The peak to valley (PV) value was used to determine the depth of the wear scars. Along with the optical microscopy images of the wear scar, which would be used to determine the length and width of the scar, the volume of lost material could be calculated. This volume (V), along with the value of sliding distance (L) and the applied force (F), could be used in the Archard wear equation to calculate wear rate (k). Equation x shows the Archard wear equation.

$$k = \frac{V}{FL} \qquad \text{Eq. 4}$$

The three samples, like their coefficients of friction, showed inverse relationships with hardness. Here, the annealed $Al_{65}Cu_{20}Fe_{15}$ showed the lowest wear rate, followed by the $Al_{50}Cu_{20}Fe_{15}$, and finally the un-annealed $Al_{65}Cu_{20}Fe_{15}$. Annealing the $Al_{65}Cu_{20}Fe_{15}$ sample led to a 12.3% reduction in wear rate, or an improvement in wear resistance. This phenomenon, like the improved hardness, is the direct result of the increased homogeneity of the sample and the increased presence of the harder

icosahedral quasicrystalline phase. Figure 37 shows the average wear rate values for all three of the samples tested.

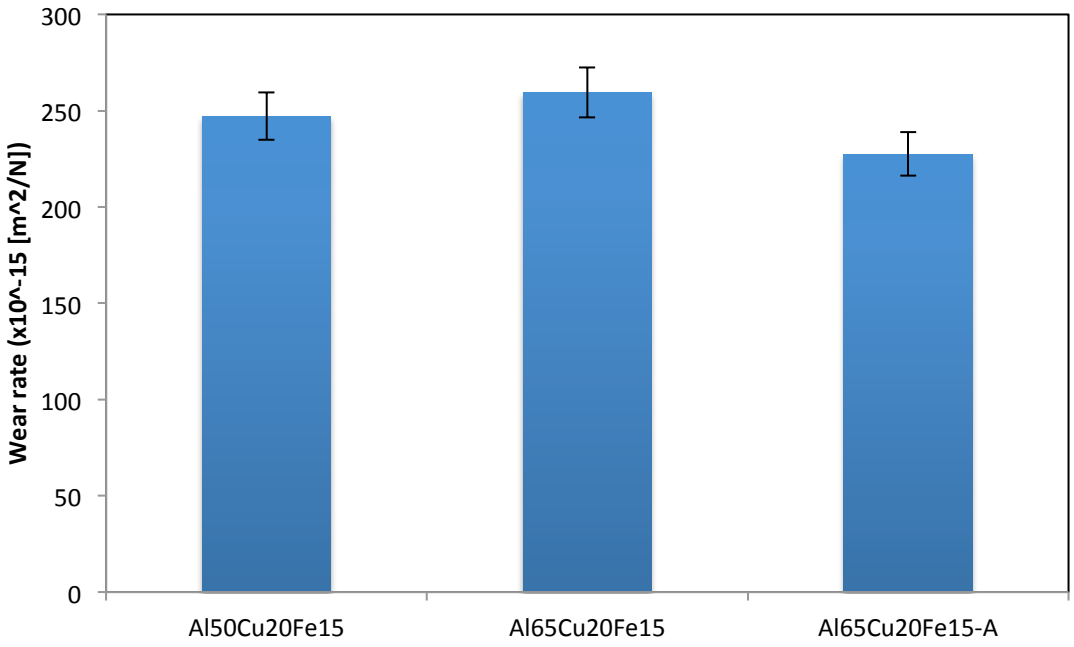

Figure 37. Wear rate results of $Al_{50}Cu_{20}Fe_{15}$, un-annealed $Al_{65}Cu_{20}Fe_{15}$, and annealed $Al_{65}Cu_{20}Fe_{15}$ alloys

4.4.3 Wear Mechanisms

The wear scars of each of the three alloy samples were evaluated to determine the mechanism by which they wore. Examples of the wear scars of $Al_{50}Cu_{20}Fe_{15}$, un-annealed $Al_{65}Cu_{20}Fe_{15}$, and annealed $Al_{65}Cu_{20}Fe_{15}$ alloys, rubbing against a stainless steel ball, may be seen in Figures 38, 39, and 40, respectively.

The wear scars created on the $Al_{50}Cu_{20}Fe_{15}$ sample showed abrasive wear to be the dominant wear mechanism. Seeing that this sample was relatively homogeneous, displaying primarily a β(τ) phase, the wear mechanism would have likely been the result of pieces of the β(τ) debris being trapped between the surface and the stainless steel ball to dig these grooves. However, there was a slight presence of the icosahedral quasicrystalline phase, which could have contributed to this wear mechanism.

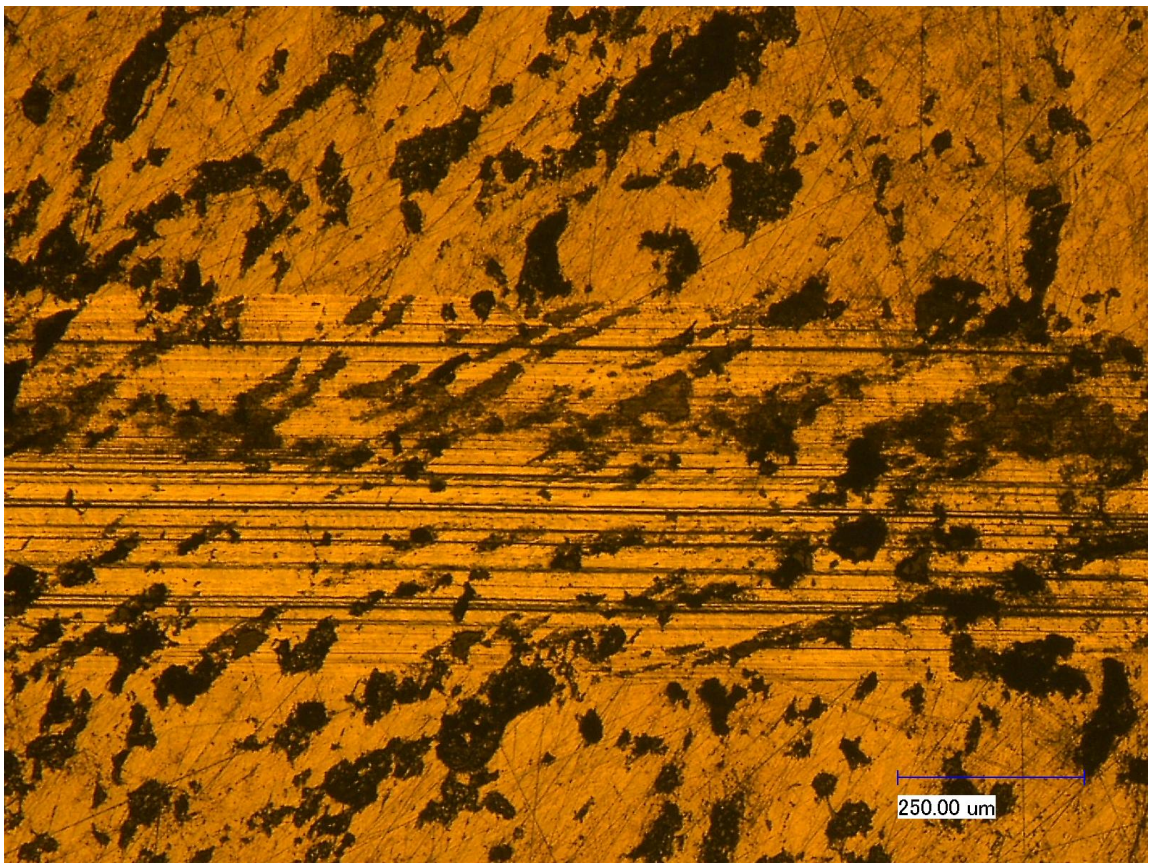

Figure 38. Wear scar of $Al_{50}Cu_{20}Fe_{15}$ in contact with SS ball

The un-annealed $Al_{65}Cu_{20}Fe_{15}$ sample did not show the porosity present in the two other samples. As Figure 39 shows, some pitting took place. Observing the deep grooves created by abrasive wear, it appears a very hard phase was the one being pulled from the material to dig these grooves into the surface. Since the icosahedral quasicrystalline phase was the hardest of the phases present, it stands to reason that this was the phase responsible for digging these grooves.

Although wear behavior of the alloy was dominated by abrasive wear, some adhesive wear did occur. Since the quasicrystalline phase exhibits too high of a hardness to deform plastically, as would be necessary in adhesive wear, it may be concluded that the observed adhesive wear is occurring along the surface of the λ and θ phases and, possibly, the β(τ) phase.

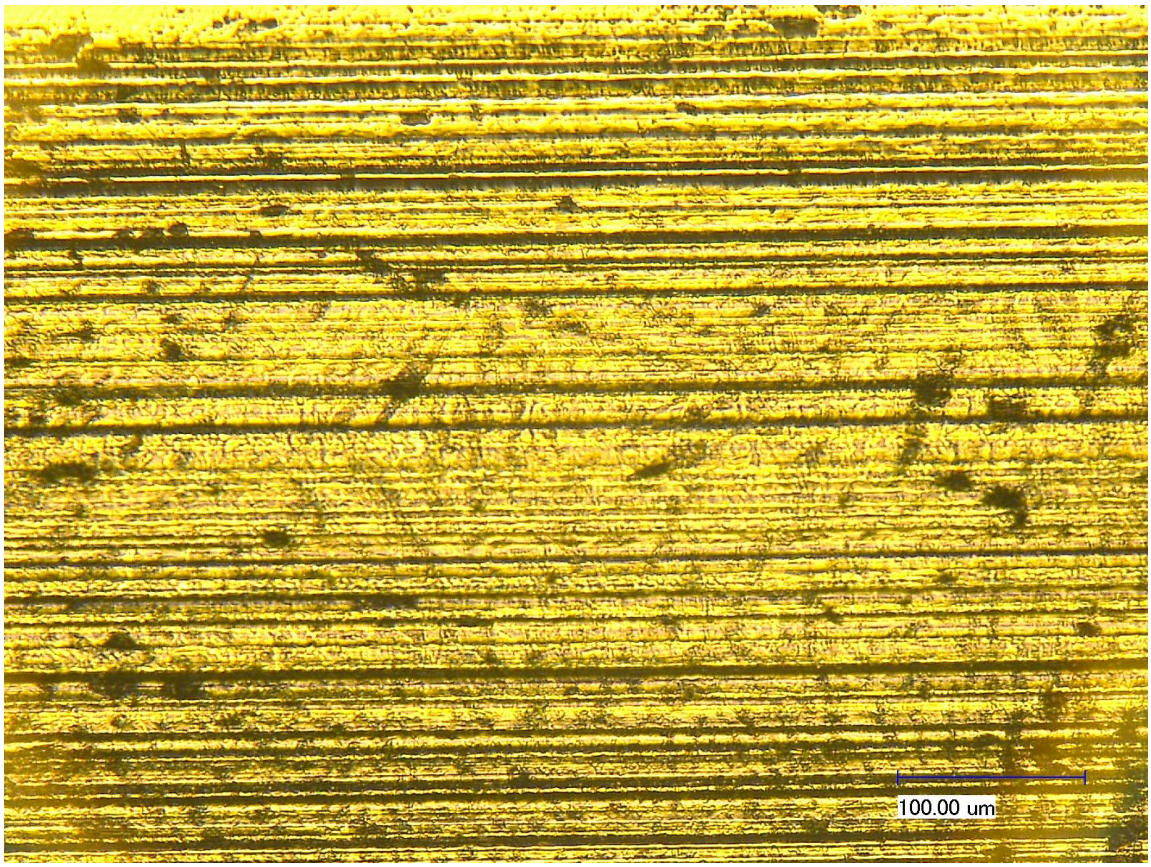

Figure 39. Wear scar of un-annealed $Al_{65}Cu_{20}Fe_{15}$ in contact with SS ball

Due to the removal of softer phases and the predominantly icosahedral quasicrystalline structure of the annealed $Al_{65}Cu_{20}Fe_{15}$ alloy, abrasive wear dominates the entire wear scar. Like the un-annealed sample, pieces of the icosahedral phase will break away and dig grooves into the material's surface, as the steel ball traps them. As this continues, material will be continually removed from the surface. Due to the harness and lower coefficient of friction of the icosahedral phase, the loss of material will be minimized, relative to the other two alloys used in this research. Adhesive wear

is no longer observed, as the presence of the more ductile phases has been minimized, and the icosahedral phase is less likely to come into contact with these phases.

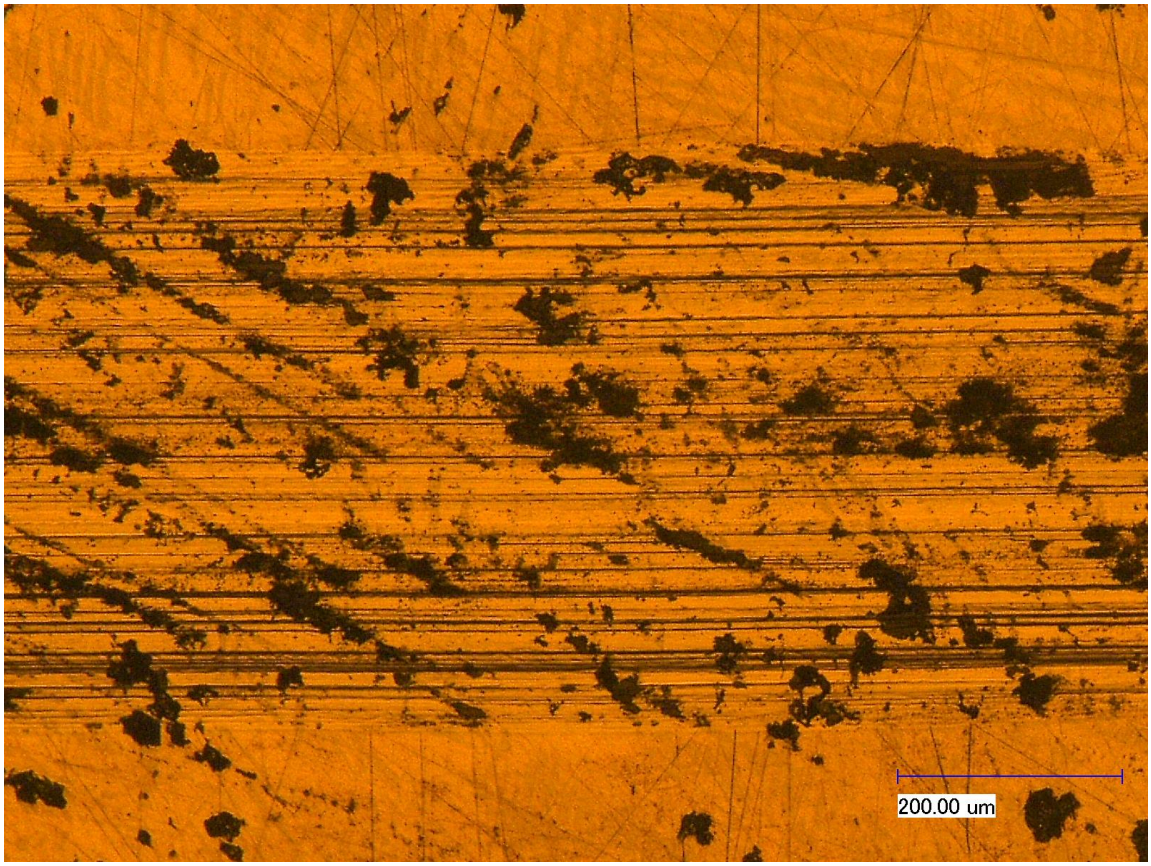

Figure 40. Wear scar of annealed $Al_{65}Cu_{20}Fe_{15}$ in contact with SS ball

CHAPTER V

UHMWPE-QUASICRYSTAL COMPOSITES

This chapter details the analysis that was conducted to examine the quality and tribological behavior of a UHMWPE-Al-Cu-Fe composite. The appearance and homogeneity of the composites were visually examined. In addition, the tribological behavior of the composites was assessed, relative to a purely UHMWPE sample.

5.1 Forming Composites

As was mentioned in the "Experimental" chapter of this paper, the UHMWPE-Al-Cu-Fe composite was formed by combining UHMWPE powders with the crushed and pulverized powders of an annealed sample of $Al_{65}Cu_{20}Fe_{15}$, in order to examine the behavior of the quasicrystalline phase in a composite. Three powder concentrations were made: (1) a completely UHMWPE sample, (2) a 20-to-1 weight concentration of UHMWPE powder to $Al_{65}Cu_{20}Fe_{15}$ powder, and (3) a 10-to-1 weight concentration of UHMWPE powder to $Al_{65}Cu_{20}Fe_{15}$ powder. These powders were thoroughly mixed by vigorously shaking the vile that contained the powders. After completing the mixing and compression molding cycle to form the composites, a visual analysis of the final samples was conducted. The three finished samples may be seen in Figure 41.

The purely UHMWPE samples had a glossy, smooth surface, and they appeared white and opaque. The samples were approximately 1 mm thick, as were the other composite samples. While the samples were stiff, they did appear to have some

flexibility. The 20-to-1 UHMWPE-$Al_{65}Cu_{20}Fe_{15}$ composite samples also exhibited a glossy, smooth surface, but they were noticeably darker. Aside from some slight aggregating of the metallic powders, the composite samples were relatively homogeneous. The 20-to-1 UHMWPE-$Al_{65}Cu_{20}Fe_{15}$ composite samples exhibited less glossy surfaces, but they were still smooth. In addition, the samples were darker, a result of the increased alloy concentration. These samples were noticeably less homogeneous than the 20-to-1 composites, as metallic particles would continually aggregate toward the outer perimeter of the sample. The increased darkness at the center of the samples is a clear indicator that the metallic powder concentration was higher than the 20-to-1 composites, but the sample appeared to become oversaturated with the powders, as the metal powders would flow outward.

Figure 41. From left to right: UHMWPE, 20-to-1 UHMWPE-$Al_{65}Cu_{20}Fe_{15}$ composite, 10-to-1 UHMWPE-$Al_{65}Cu_{20}Fe_{15}$ composite

It was important for the Al-Cu-Fe powders to be relatively fine, in order to avoid surface irregularity effects in the tribometry tests of the composites. In addition, a fine powder was necessary to increase the contact area between the metallic powders and the

polymer powders. This would affect bonding forces between the particles and affect the homogeneity of a composite sample.

From Figure 42, the size of the Al-Cu-Fe particles may be seen. An optical microscope generated this image. It may be seen that the powders could vary in size considerably. Most of the particles were within a range of 1 μm to 8 μm in diameter. Though it would be optimal for each of the particles to be less than 1 μm in size, the occasionally occurrence of a larger particle should not drastically alter the composites' performance. Nonetheless, further, more thorough pulverizing of the powders should be conducted in future research to guarantee the minimization of any of the negative effects brought on by the large particle size of metallic powders.

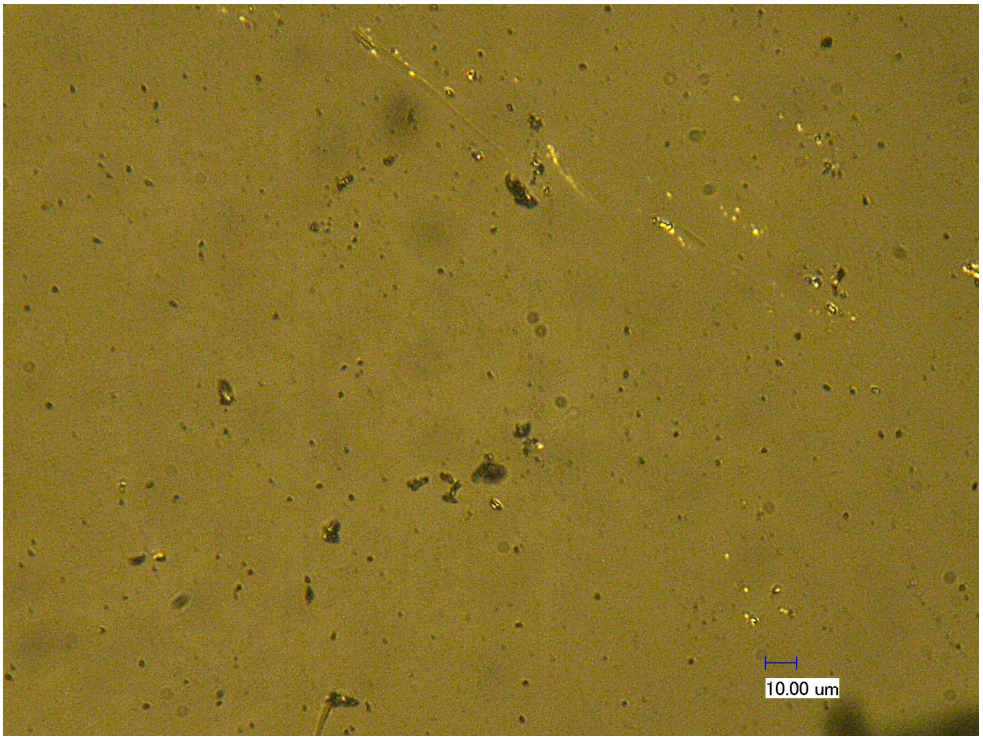

Figure 42. Al-Cu-Fe powders images from optical microscope

5.2 Tribological Performance

It was desirable to evaluate the friction behavior of these composite samples, in contact with a stainless steel ball, as their friction behavior is critical to understanding their ability to be used in biomedical and general coating applications. It was observed that the coefficient of friction for each of the samples would steadily drop, in a manner similar to an exponentially decaying function, after which the value would remain constant. This constant value was used to determine the coefficient of friction for the corresponding sample, as a contributing value to an average from 5 to 6 tests. Examples of the individual coefficients of friction from the UHMWPE, 20-to-1 UHMWPE-$Al_{65}Cu_{20}Fe_{15}$ composite, and 10-to-1 UHMWPE-$Al_{65}Cu_{20}Fe_{15}$ composite may be seen in Figure 43. The average coefficient of friction data for the three samples is displayed in Figure 44.

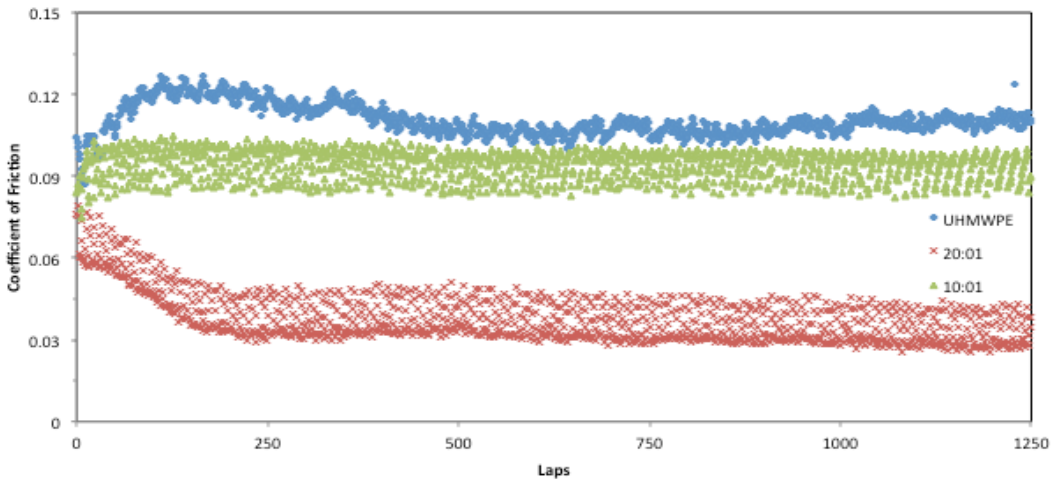

Figure 43. The coefficient of friction for purely UHMWPE sample, a 20-to-1 UHMWPE-$Al_{65}Cu_{20}Fe_{15}$ composite, a 10-to-1 UHMWPE-$Al_{65}Cu_{20}Fe_{15}$ composite

In the case of the UHMWPE sliding against the stainless steel ball, the coefficient of friction value (0.11) was in range of normally published values for similar tests. With the addition of the Al-Cu-Fe quasicrystalline powders to the UHMWPE in the 20-to-1 composite, a drastic decrease in the coefficient of friction was observed (70%). As the concentration of metallic powders increased, the improvement in friction coefficient became less pronounced. As was previously mentioned, the 10-to-1 composite samples appeared to become oversaturated, and metallic powders would flow to the outer perimeter of the samples. As a result, more aggregation of metallic powders is likely to have occurred. Relatively large irregularities at the sample surface would increase the coefficient of friction, due to large pieces of metal being pulled from the matrix, being dragged at the interface of the sample and stainless steel ball, and creating a more rugged surface.

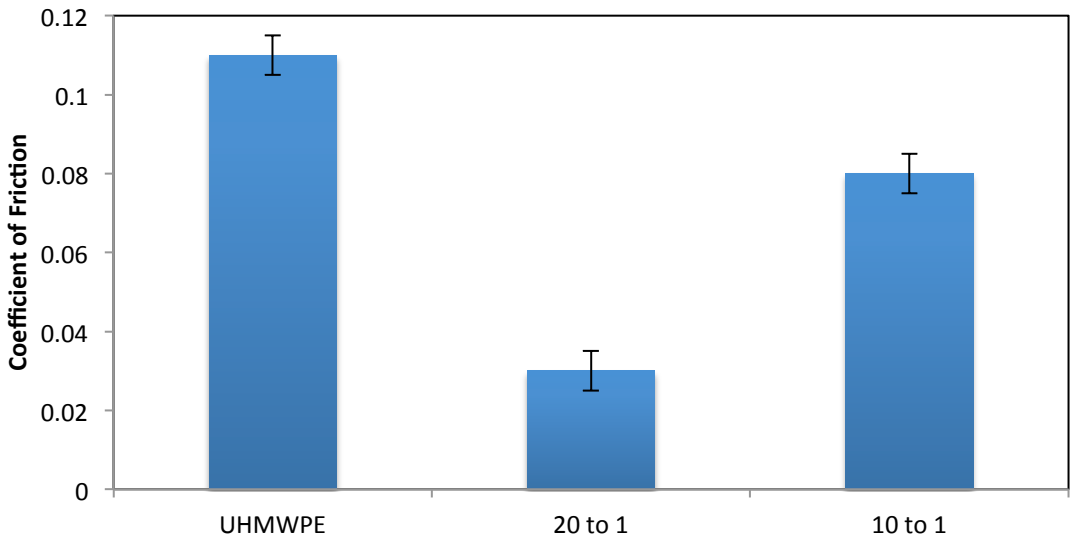

Figure 44. Coefficients of friction for purely UHMWPE sample, a 20-to-1 UHMWPE-$Al_{65}Cu_{20}Fe_{15}$ composite, a 10-to-1 UHMWPE-$Al_{65}Cu_{20}Fe_{15}$ composite

Finally, a measure of wear rate was evaluated by modifying the tribometer for a homemade scratch test. Instead of the stainless steel ball, a carbon-steel nail was dragged along the surfaces of the samples. The half-amplitude of the wear track was 1 mm long, and the test was allowed to run over a total distance of 20 cm. A load of 3 N was used, and the speed of the tribometer was set to 0.9 cm/s. The wear rate, here, was measured as the depth of the resulting scar. To measure the depth of this scar, the sample was cut along the transverse axis of the scar, through its middle point. The sample was then viewed underneath an optical microscope to visually inspect this depth. Figure 45 shows an example of one of these images, taken of the 20-to-1 UHMWPE-$Al_{65}Cu_{20}Fe_{15}$ composite. Figure 46 shows the mean values of the scar depth for the three samples.

Figure 45. Example of cross-section of scratch scar for evaluating wear rate

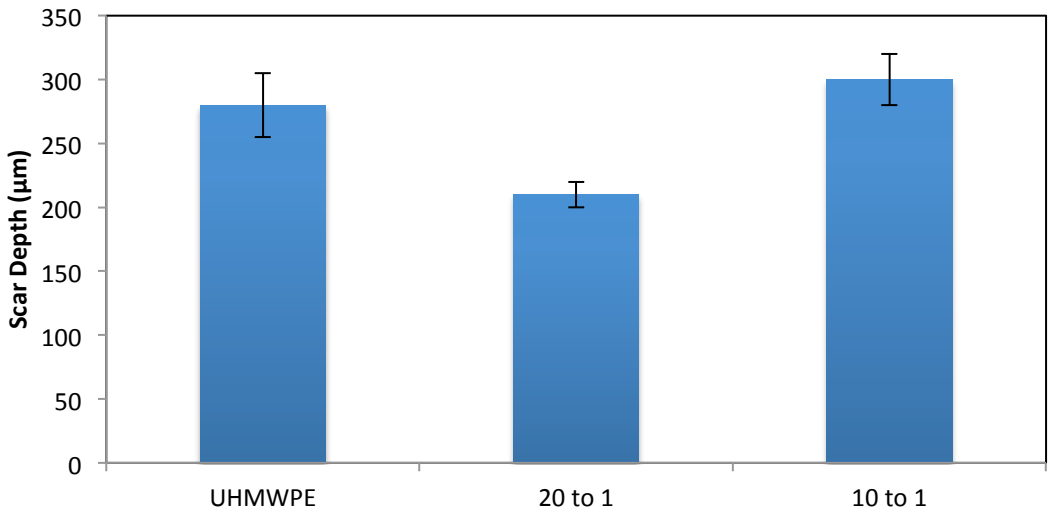

Figure 46. Average scar depth values for purely UHMWPE sample, a 20-to-1 UHMWPE-$Al_{65}Cu_{20}Fe_{15}$ composite, a 10-to-1 UHMWPE-$Al_{65}Cu_{20}Fe_{15}$ composite

In the case of a 20-to-1 UHMWPE-$Al_{65}Cu_{20}Fe_{15}$ composite, the wear resistance improved noticeably, compared to the purely UHMWPE sample. This effect, however, was not observed in the sample containing a higher concentration of the quasicrystalline particles. As was previously mentioned, this sample appeared less homogeneous, so the aggregation of quasicrystalline particles was more likely to take place. This would cause the large pieces to be dragged through the sample, when contacted by the sharp tip of the nail, which would more rapidly remove material during the test.

CHAPTER VI

CONCLUSION

6.1 Conclusions

The research presented in this thesis investigated a novel approach for the fabrication of a composite material, using the relatively new class of quasicrystalline materials. After preparing the alloys by arc melting, their material properties were analyzed, as well as their mechanical and tribological behavior. Finally, they were crushed and added to a UHMWPE matrix to form a compression-molded composite. Some observations and conclusions were made throughout this process.

- The annealing process improved the hardness of the $Al_{65}Cu_{20}Fe_{15}$ alloy by increasing the presence and homogeneity of the quasicrystalline phase and reducing the presence of crystalline phases. Annealing the $Al_{65}Cu_{20}Fe_{15}$ sample led to about a 20% increase in the icosahedral quasicrystalline phase and a decrease in hardness by 8%, showing the benefit of a purely quasicrystal alloy.
- Wear rate correlated inversely with hardness across all samples, where a higher hardness meant a lower wear rate. Comparing the un-annealed and annealed $Al_{65}Cu_{20}Fe_{15}$ samples, an increase in hardness by 8% corresponded to a decrease in wear rate by 12.3%.
- The annealed and predominantly quasicrystalline $Al_{65}Cu_{20}Fe_{15}$ sample showed an abrasive wear mechanism, as pieces from the hard quasicrystalline phase broke away from the material and dug grooves into the surface.

- Quasicrystalline alloys were successfully pulverized into powders, ranging in size from 1 μm to 8 μm, and they were added to UHMWPE to form relatively homogeneous composite materials.
- The friction coefficient of UHMWPE was reduced with the addition of the quasicrystalline alloy powders, though increasing the alloy content too much in the composite lessened this effect.
- The wear rate of UHMWPE, as a measure of scar depth, was reduced with the addition of the quasicrystalline alloy powders, but the addition of too much of these powders would lead to the increase in the wear rate of UHMWPE.
- Increasing the alloy presence led to less homogeneous composites, so clumping of metal powders may have created rougher portions on the surface and increased the coefficient of friction.

6.2 Future Work and Recommendations

In addition to the conclusions that were drawn from the experiments, some further work should be conducted to improve the understanding of these materials. Some of the work and recommendations to be considered are discussed here.

- Composites containing purely icosahedral quasicrystal powders, which may be formed by using a longer/adjusted annealing cycle, should be made and tested to evaluate their performance.

- A more automated process should be considered for crushing and pulverizing the Al-Cu-Fe powders, in order to further simplify the process of making these composite materials.
- A more thorough investigation into the UHMWPE-to-Al-Cu-Fe powder concentrations should be conducted, in order to determine the optimal balance of matrix and microconstituent materials.
- More tests should be conducted to evaluate the mechanical and chemical properties and tribological behavior of the composites, as these metrics would all provide a clearer understanding of the composites' mechanical and tribological behavior.
- The toxicity and biocompatibility of the composites should be thoroughly investigated, in order to continue to prove the practicality of this material in biomedical applications.

REFERENCES

1. I. El-Said, A.P., *Geometric Concepts in Islamic Art*, in *World of Islam Festival*1976: London. p. 85-87.
2. P.J. Lu, P.J.S., *Decagonal and Quasi-Crystalline Tilings in Medieval Islamic Architecture.* Science, 2007. **315**: p. 1106-1110.
3. Penrose, R., *The role of aesthetics in pure and applied mathematical research.* Bulletin of the Institute of Mathematics and its Applications, 1974. **10**: p. 266-271.
4. Mackay, A.L., *What has Penrose tiliing to do with the icosahedral phases? Geometric aspects of the icosahedral quasicrystal problem.* Journal of Microscopy, 1987. **146**: p. 233-243.
5. D. Shechtman, I.B., D. Gratias, J.W. Cahn, *Metallic Phase with Long-Range Orientational Order and No Translational Symmetry.* Physical Review Letters, 1984. **53**: p. 1951-1953.
6. T. Ishimasa, H.U.N., Y. Fukano, *New Ordered State Between Crystalline and Amorphous in Ni-Cr Particles.* Physical Review Letters, 1985. **55**: p. 511-513.
7. A.J. Bradley, H.J.G., *An X-ray study of slowly cooled iron-copper-aluminum alloys. Part II. Alloysrich in aluminum.* Journal of the Institute of Metals, 1939. **65**: p. 403-418.
8. A.P. Tsai, A.I., T. Masumoto, *A stable quasicrystal in Al-Cu-Fe system.* Journal of Applied Physics, 1987. **26**: p. L1505-L1507.

9. A. Yamamoto, H.T., A.P. Tsai, *Refinement of i-Al-Cu-Fe and i-Al-Cu-Ru Quasicrystal Structures.* Ferroelectrics, 2004. **305**: p. 279-282.

10. L. Bindi, P.J.S., *The discovery of the first natural quasicrystal.* Elements, 2012(February): p. 13-14.

11. Katz, A., *Aperiodicity and Order*. Introduction to the mathematics of quasicrystals, ed. M.V. Jaric. Vol. 2. 1989, New York, NY: Academic Press.

12. J. Tang, X.Z., D. Zhao, G.Q. Lu, J. Zou, C. Yu, *Hard-Sphere Packing and Icosahedral Assembly in the Formation of Mesoporous Materials.* Journal of the American Chemical Society, 2007. **129**: p. 9044-9048.

13. J.E. Shield, J.A.C., *Mechanical properties of Al-Cu-Fe-based quasicrystalline coatings.* Journal of Materials Science Letters, 1997. **16**: p. 2019-2021.

14. J.M. Dubois, S.S.K., A. Perrot, *Towards applications of quasicrystals.* Materials Science and Engineering, 1994. **A179/A180**: p. 122-126.

15. B.C. Anderson, P.D.B., K.G. Baikerikar, V.V. Sheares, S.K. Mallapragada, *Al–Cu–Fe quasicrystal/ultra-high molecular weight polyethylene composites as biomaterials for acetabular cup prosthetics.* Biomaterials, 2002. **23**: p. 1761-1768.

16. M.L. Wilson, S.L., R.M. Stroud, T.M. Tritt, *Measurement of the Thermoelectric Properties of Quasicrystalline AlPdRe and AlCuFe Alloys.* MRS Proceedings, 1997. **478**: p. 321.

17. Beardsley, M.B., *Potential use of quasicrystalline materials as thermal barrier coatings for diesel engine components*, in *Materials Science and Engineering*2008, Iowa State University: Ames, IA.

18. C. Amuwu, L.D.D., *The Combined Anteversion Technique for Acetabular Component Anteversion.* Journal of Arthroplasty, 2008. **23**(7).

19. S. Yin, Q.B., L. Qian, A. Zhang, *Formation of Al70Cu20Fe10 icosahedral quasicrystal by mechanically alloyed method.* Materials Science and Engineering, 2007. **465**: p. 95-99.

20. B.S. Murty, R.V.K.R., N.K. Mukhopadhyay, *Stability of quasicrystalline phase in Al–Cu–Fe, Al–Cu–Co and Al–Pd–Mn systems by high energy ball milling.* Journal of Non-Crystalline Solids, 2004. **334&335**: p. 48-51.

21. Bokhonov, B.B., *Mechanical alloying and self-propagating high-temperature synthesis of stable icosahedral quasicrystals.* Journal of Alloys and Compounds, 2008. **461**: p. 150-153.

22. P. Barua, B.S.M., B.K. Mathur, V. Srinivas *Nanostructured icosahedral phase formation in Al70Cu20Fe10 by mechanical alloying: Comprehensive study.* Journal of Applied Physics, 2002. **91**: p. 5353-5359.

23. S. Yin, Z.X., Q. Bian, B. He, Z. Pan, Z. Sun, Z. Wei, L. Qian, S. Wei, *Formation of AlCuFe icosahedral quasicrystal by mechanical alloying: XAFS and XRD studies.* Journal of Alloys and Compounds, 2008. **455**: p. 314-321.

24. W.D. Yuan, T.M.S., E. Fleury, D. Se, D.R. Chen, *Microstructure and tribological properties of plasma sprayed Al–Cu–Fe quasicrystalline coatings*

after laser post-treatment processing. Surface and Coating Technology, 2004. **185**: p. 99-105.

25. K. Biswas, R.G., B.L. Mordike, K. Chattopadhyay, *Laser cladding of quasicrystal forming Al–Cu–Fe on aluminum.* Journal of Non-Crystalline Solids, 2004. **334&335**: p. 517-523.
26. K. Chattopadhyay, K.B., S. Bysakh, G. Phanikumar, A. Weisheit, R. Galurn, B.L. Mordike, *Quasicrystalline coatings through laser processing: A study on process optimization and microstructure evolution*, in *MRS Proceedings*2001. p. K15.3.1-K15.3.12.
27. M.A. Suarez, R.E., J. Alcantara, H. Dorantes, J.F. Chavez, *Effect of chemical composition on the microstructure and hardness of Al–Cu–Fe alloy.* Materials Characterization, 2011. **62**: p. 917-923.
28. J. Quispe-Marcatoma, C.R.-A., C.V. Landauro, M.A. de Sousa, F. Pelegrini, M. Taquire, V.A. Pena Rodriguez, E.M. Baggio-Saitovich, *Nanostructuration of i-Al64Cu23Fe13 quasicrystals produced by arc-furnace.* Hyperfine Interact, 2011. **203**: p. 1-8.
29. X. Yong, I.T.C., I.P. Jones, *Formation of a quasicrystalline phase in mechanically alloyed Al65Cu25Fe15.* Journal of Alloys and Compounds, 2005. **387**: p. 128-133.
30. B. Grushko, T.V., *Formation of quasiperiodic and related periodic intermetallics in alloy systems of aluminum with transition metals.* Computing Coupling of Phase Diagrams and Thermochemistry, 2007. **31**: p. 217-232.

31. F.P. Bowden, D.T., *Friction: an introduction to tribology*. 1973, Garden City, NY: Anchor Press.

32. Blau, P.J., *Friction Science and Technology: From Concepts to Applications, 2nd Edition*. 2010: CRC Press.

33. Rabinowicz, E., *Friction and Wear of Materials*. 1995, New York: John Wiley and Sons.

34. Archard, J.F., *Contact and Rubbing of Flat Surfaces.* Journal of Applied Physics, 1953. **24**: p. 981.

35. McKellop, H.A., *Wear modes, mechanisms, damage and debris: Separating cause from effect in the wear of total join replacements*. Total Hip Revision Surgery, ed. A.G.R. O. Galante, J.J. Callaghan. 1995, New York, NY: Raven Press.

36. T.P. Schmalzreid, J.J.C., *Current concepts reviews: Wear in total hip and knee replacements.* Journal of Bone and Joint Sugery, 1999. **81**: p. 115-136.

37. A.S. Litsky, M.S., *Orthaopaedic Basic Science*. Biomaterials, ed. S. SR. 1994, Rosemont, IL: American Academy of Orthopaedic Surgeons.

38. K. Holmberg, H.R., A. Laukkanen, K. Wallin, *Friction and wear of coated surfaces - scales, modelling, and simulation of tribomechanisms.* Surface and Coating Technology, 2007. **202**: p. 1034-1049.

39. Gahr, K.-H.Z., ed. *Microstructure and Wear of Materials*. Tribology Series. Vol. 10. 1987, Elsevier.

40. B.H. Currier, J.H.C., M.B. Mayor, K.A. Lyford, J.P. Collier, D.W. Van Citters, *Evaluation of Oxiation and Fatigue Damage of Retrieved Crossfire Polyethylene Acetabular Cups.* Journal of Bone and Joint Sugery, 2007. **89**: p. 2023-2029.

41. R.P. Schaake, J.M.J.d.T., W.P. Vellinga, H.E.H. Meijer, *One-Minute Wear-Rate Measurement.* Macromolecular Rapid Communications, 2005. **26**: p. 188-191.

42. W. Shi, H.D., T. Bell, *Tribological behaviour and microscopic wear mechanisms of UHMWPE sliding against thermal oxidation-treated Ti6Al4V.* Materials Science and Engineering, 2000. **A291**: p. 27-36.

43. B. Panjwani, N.S., S.K. Sinha, *Tribological characterization of a biocompatible thin film of UHMWPE on Ti6Al4V and the effects of PFPE as top lubricating layer.* Journal of the Mechanical Behavior of Biomedical Materials, 2011. **4**: p. 953-960.

44. J.M. Dowling, J.R.A., D. Dowson, J. Charnley, *The Characteristics of Acetabular Cups Worn in the Human Body.* Journal of Bone and Joint Sugery, 1978. **60**: p. 375-382.

45. T.P. Schmalzreid, M.J., A. Rosenberg, W.H. Harris, *Polyethylene Wear Debris and Tissue Reactions in Knee as Compared to Hip Replacement Prostheses.* Journal of Applied Biomaterials, 1994. **5**: p. 185-190.

46. R.M. Rose, H.J.H., H. Schneider, M. Ries, I. Paul, A. Crugnola, S.R. Simon, E.L. Radin, *On the True Wear Rate of UHMWPE in the Total HIp Prosthesis.* 1980, 1980. **62A**: p. 537-549.

47. M. Jasty, C.B., K. Lee, W.H. Harris, *Wear of Polyethylene in Total Joint Arthroplasty.* Seminars in Arthroplasty, 1994. **5**: p. 41-44.

48. S.L. Smith, H.E.A., A. Unsworth, *A tribological study of UHMWPE acetabular cups and polyurethane compliant layer acetabular cups.* Journal Of Biomedical Material Research, 2000. **53**: p. 710-716.

49. A. Barneston, P.R.H., *Observations on the sintering of Ultra-high Molecular Weight Polyethylene (UHMWPE) Powders.* Journal of Materials Science Letters, 1995. **14**: p. 80-84.

50. Z.G. Wang, B.S.H., N. Stribeck, R. Gehrke, *Nanostructure Evolution of Isotropic High-Pressure Injection-Molded UHMWPE during Heating.* Macromolecules, 2002. **35**: p. 2200-2206.

51. E. Puukilainen, H.S., T.A. Pakken, *Compression-Molded, Lubricant-Treated UHMWPE Composites.* J. Applied Polymer Science, 2007. **104**: p. 1762-1768.

52. M. Abdul Samad, S.K.S., *Dry sliding and boundary lubrication performance of a UHMWPE/CNTs nanocomposite coating on steel substrates at elevated temperatures.* Wear, 2011. **270**: p. 395-402.

53. C.J. Schwartz, S.B., S.K. Mallapragada, *Effect of crosslinking and Pt–Zr quasicrystal fillers on the mechanical properties and wear resistance of UHMWPE for use in artificial joints.* Wear, 2007. **263**: p. 1072-1080.

54. J. Yang, F.G., *First principles calculations of mechanical properties of cubic 5d transition metal monocarbides.* Physica B, 2012. **407**: p. 3527-3534.